Experimental and Theoretical Investigation of the Restructuring Process Induced by CO at Near Ambient Pressure: Pt Nanoclusters on Graphene/Ir(111)

Nicola Podda,[†] Manuel Corva,[†,‡] Fatema Mohamed,[†,§] Zhijing Feng,[†,‡] Carlo Dri,[†,‡] Filip Dvorák,[‖] Vladimir Matolin,[‖] Giovanni Comelli,[†,‡] Maria Peressi,[†,‡] and Erik Vesselli*,[†,‡]

[†]Physics Department, University of Trieste, via A. Valerio 2, Trieste 34127, Italy
[‡]Istituto Officina dei Materiali CNR-IOM, S.S. 14 km 163.5, Area Science Park, Basovizza ,Trieste 34149, Italy
[§]International Centre for Theoretical Physics ICTP, Strada Costiera 11, Trieste 34151, Italy
[‖]Faculty of Mathematics and Physics, Charles University in Prague, V Holešovickách 2, Praha 8 180 00, Czech Republica

S *Supporting Information*

ABSTRACT: The adsorption of CO on Pt nanoclusters grown in a regular array on a template provided by the graphene/Ir(111) Moiré was investigated by means of infrared-visible sum frequency generation vibronic spectroscopy, scanning tunneling microscopy, X-ray photoelectron spectroscopy from ultrahigh vacuum to near-ambient pressure, and *ab initio* simulations. Both terminally and bridge bonded CO species populate nonequivalent sites of the clusters, spanning from first to second-layer terraces to borders and edges, depending on the particle size and morphology and on the adsorption conditions. By combining experimental information and the results of the simulations, we observe a significant restructuring of the clusters. Additionally, above room temperature and at 0.1 mbar, Pt clusters catalyze the spillover of CO to the underlying graphene/Ir(111) interface.
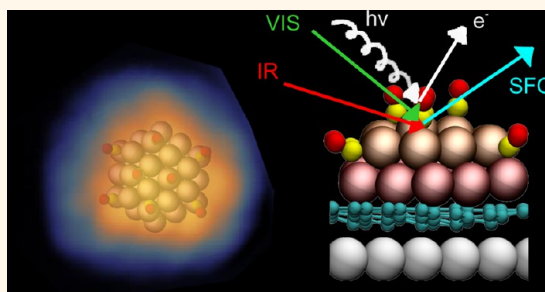
KEYWORDS: *graphene, platinum clusters, carbon monoxide, SFG, near-ambient pressure*

Small metallic clusters are known to display structural, electronic, and chemical properties that are peculiar with respect to the corresponding bulk analogues.[1,2] Quantum-size effects may even yield nonmetallic behavior, and the availability of reactive under-coordinated sites makes cluster-based catalytic systems of widespread interest. In the case of platinum, highly active and selective catalysts for the oxidation of propane have been successfully engineered on SnO and Al_2O_3 supports by exploiting few atom Pt nanoparticles.[1] Pt concave sites are found to be very active for oxygen reduction, while isolated single Pt atoms play an important role in CO oxidation and in water−gas shift reactions.[3−5] For these applications, the practical realization of stable systems with very precise control on the clusters size distribution is extremely important.[6] In this view, the support has a fundamental role for the growth and anchoring of the metal particles, and important research efforts are dedicated to the investigation of optimal templates within the families of both oxides and supported graphene (GR).[7,8] More specifically, the weakly interacting GR/Ir(111) system is one of the most studied models since the Moiré-induced geometric and chemical corrugation of GR, caused by the lattice mismatch with the underlying Ir termination, provides an optimal template on which metal particles can be grown in an essentially regular hexagonal array. Physical vapor deposition of Pt atoms at room temperature yields a self-assembled cluster lattice, with particles adsorbed in the hcp sites of the GR Moiré unit cell and stable up to 400 K for small sizes and up to 650 K for large sized particles.[7,9] Deposition of 0.05 ML Pt/GR/Ir(111) yields the development in the C 1s core level spectra of a broad shoulder at the higher binding energy side of the main graphene peak.[10] The GR sheet undergoes deformation due to the cluster pinning, yielding a sp^2 to sp^3 rehybridization of GR carbon atoms squeezed at the Pt−Ir interface.[11] The main graphene C 1s peak is also shifted by +50 meV with respect to the bare sheet, due to Pt doping. Upon exposing the clusters to
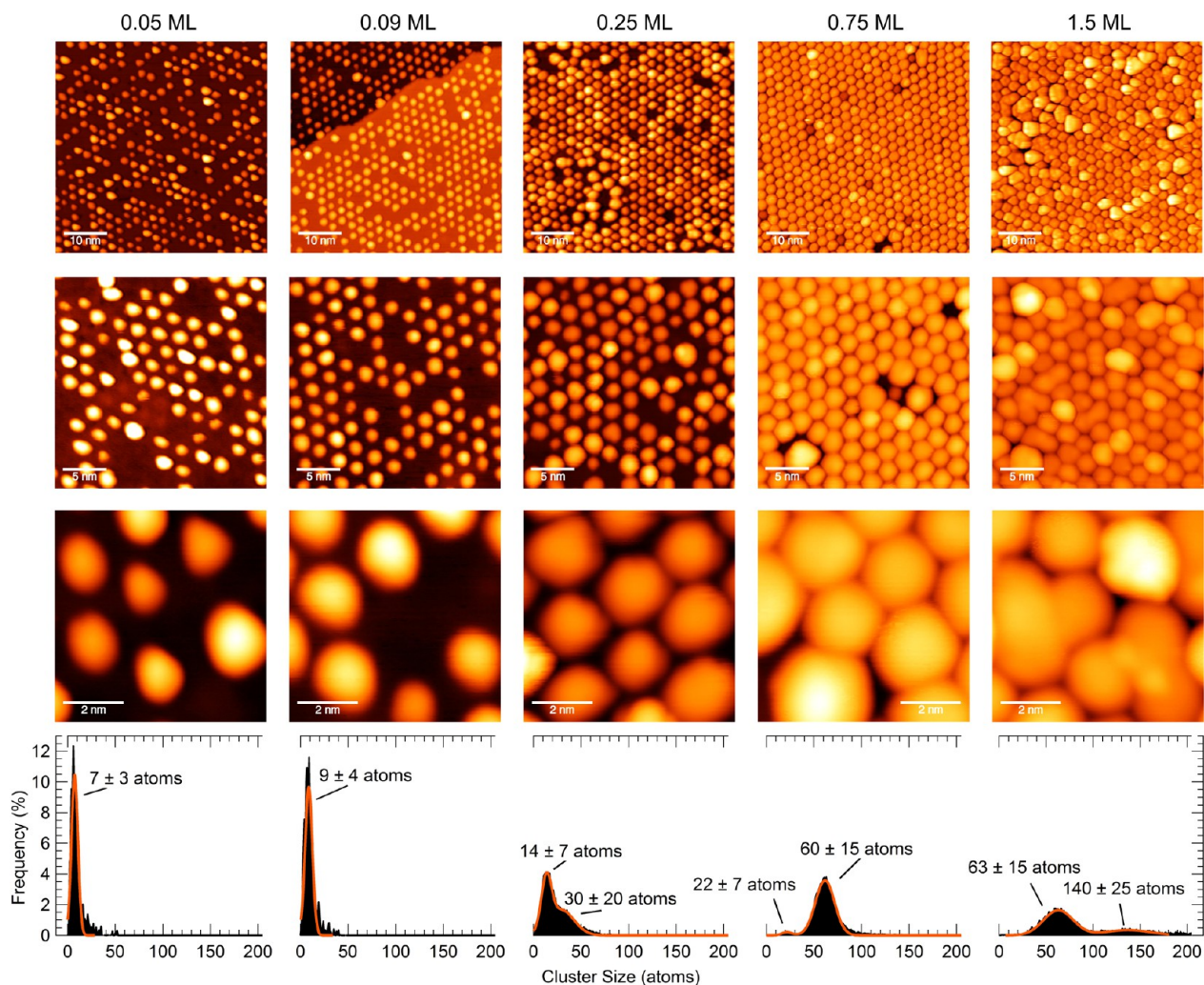
1

Figure 1. Selected STM images collected at 77 K after depositing Pt at room temperature on a single graphene layer on Ir(111). Pt loadings span from 0.05 to 1.5 ML (from left to right), and different image sizes are shown (from top to bottom: 50×50, 25×25, and 7×7 nm^2, respectively; V_{bias} = +1.0 V, I = 20−100 pA depending on image). In the bottom panel, corresponding size distributions (cluster size frequencies) are shown as obtained upon averaging the whole STM image data set: continuous lines represent fitting curves with Gaussian profiles (position and width of the peaks are reported in the text labels).

10 L of CO, the rehybridization shoulder diminishes in intensity, and the main C 1s peak shifts back to its original position. Clusters formed by <10 atoms are unstable upon CO sticking and diffuse and coalesce, yielding a Smoluchowski ripening effect.[10] A time-resolved investigation reveals that the aforementioned changes in the spectroscopic signals set in already before the onset of clusters mobility. Therefore, CO adsorption influences the graphene rehybridization beneath the clusters before sintering. However, it is found that CO adsorption at on-top Pt sites does not compete for the same electronic density involved in the binding of Pt to the GR support, which takes place through the Pt($5d_{3z^2-r^2}$)-C($2p_z$) interaction. Instead, density functional theory (DFT) calculations ascribe the observed mobility to the adsorption of CO in bridge Pt sites at the borders of the clusters. However, population of bridge sites was not observed under ultrahigh vacuum (UHV) conditions,[10] at variance with the Pt/GR/Rh(111) case,[12] thus leaving this issue partly unsolved. X-ray diffraction measurements of the Pt/GR/Ir(111) system upon exposure to 10^{-7} mbar CO followed by 10^{-6} mbar O$_2$ show a CO-induced reversible breathing-like transformation of the nanoparticles.[13] Due to the applicative potential of GR-

supported Pt catalysts, the morphological changes induced by adsorption are a crucial issue and have therefore been thoroughly investigated under vacuum conditions,[7,10,12−14] while for Pt single crystal terminations, CO adsorption has been investigated also in the near-ambient pressure (NAP) regime.[15,16]

In the present paper, we report a combined spectroscopic, microscopic, and theoretical investigation of the adsorption of CO on the Pt clusters grown on GR/Ir(111) at pressures from UHV up to 1 mbar. We provide evidence for the adsorption of CO in both top and bridge configurations on Pt clusters, with the population of several nonequivalent sites, spanning from first to second-layer terraces to borders and edges, depending on the particle size and morphology and on the adsorption conditions. Upon heating above 420 K, CO spillover to the underlying Ir(111) surface is observed, catalyzed by the presence of the Pt particles.

RESULTS AND DISCUSSION

The Pt/GR/Ir(111) system is already well-known in literature and has been experimentally and theoretically investigated by

means of a number of techniques.[7−13] In order to thoroughly characterize the ordered array of Pt nanoparticles for the adsorption of CO, we first applied the known growth recipes by evaporating Pt atoms from the physical vapor phase on the graphene Moiré at room temperature. Different methods for the calibration of the Pt coverage were adopted, depending on the experimental setup (details in the Methods section). By means of STM, we characterized the size distributions of the clusters for selected Pt loadings, namely 0.05, 0.09, 0.25, 0.75, and 1.5 ML (throughout the manuscript, the monolayer coverage calibration refers to the underlying Ir(111) metal surface). Our results are both qualitatively and quantitatively in agreement with recent literature concerning the cluster morphology and the Moiré filling factor,[14] thus providing a reliable starting point for the characterization at NAP conditions. In Figure 1, we plot a set of STM images with different lateral scales (from top to bottom: 50 × 50, 25 × 25, and 7 × 7 nm^2) for the five coverage values, together with the distributions of the cluster dimensions (bottom). The actual number of atoms was obtained in the following way: the apparent volume of each cluster, which depends on the shape and the electronic structure of the cluster itself and of the STM tip, was extracted by means of 2D profiling and z-cutting of the images, followed by a renormalization to the nominal Pt coverage. The latter was calibrated by imaging Pt ad-islands on the bare Ir(111) clean surface, in analogy to previous literature.[8] For Pt loadings below a quarter of a monolayer, the cluster size distribution is found to be unimodal, with a single peak at 7 and 9 atoms per cluster for 0.05 and 0.09 ML Pt, respectively (Figure 1, bottom, and Figure 2c). The Moiré filling factor (Figure 2a) grows rapidly to 80%, and the superlattice mainly consists of single-layer clusters (Figure 2b). At 0.25 ML, 1- and 2-layer clusters coexist, with (average) sizes of 14 and 30 atoms, respectively, and almost saturate the Moiré, the distribution of the sizes becoming bimodal. This peculiar feature of the cluster size distribution was not reported in previous literature.[10,14] Interestingly, each of the families of the largest clusters (0.25, 0.75, and 1.5 ML Pt) shows a size distribution with two peaks, the second positioned at about twice the size of the first one (as evident both in Figure 1, bottom, and in Figure 2d). This suggests that the largest clusters for each Pt loading originate from the coalescence of two adjacent smaller particles. The dashed line in Figure 2d indicates the nominal cluster size as a function of the Pt coverage, i.e., the number of Pt atoms forming the clusters in the case in which all the clusters were identical with a unity Moiré filling factor. If the nominal size for small clusters is rescaled with the observed, experimental filling factor, the agreement between expected and measured average size is excellent. Indeed, we get coincident expected and experimental average cluster sizes of 7 and 9 atoms for 0.05 and 0.09 ML Pt, respectively. For 0.25 ML Pt, we get instead 21 atoms, which is about the average between the observed experimental sizes of the bimodal distribution (14 and 30 atoms). From the ab initio calculations in the reduced models we found that for Pt$_n$ nanoclusters with $n > 7$, the aggregation in the hcp region is preferred (by 0.2 eV for Pt$_9$: $E_{ads\ hcp}$ = 10.43 eV, $E_{ads\ fcc}$ = 10.23 eV), but for smaller nanoclusters, there is no preference between the two regions. These findings suggest high mobility of very small Pt aggregates and are consistent with the absence of nanoclusters with $n < 5$ in the experimental observation, even at very low coverage. From the experiments at 0.75 ML, 100% of the Moiré hcp sites are mostly populated by 2-layer
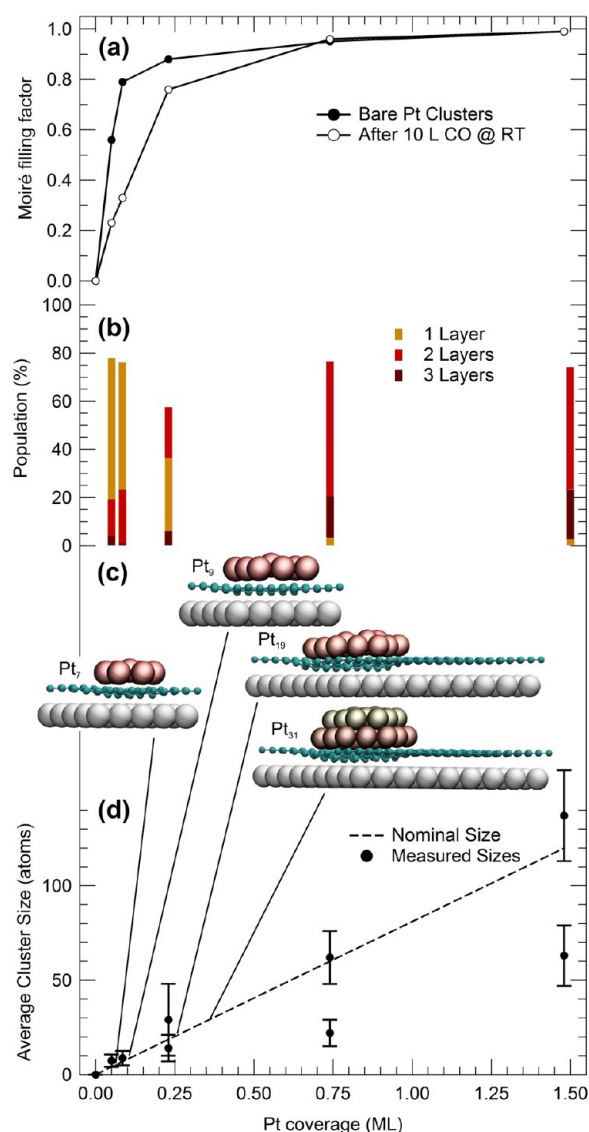

Figure 2. (a) Moiré filling factor prior and after exposure of the Pt clusters to 10 L CO at room temperature. (b) Cluster height population of the bare Pt clusters (the bars are intended to start from zero and have been overlapped). (c) Fully relaxed DFT models for clusters of 7, 9, 19, and 31 Pt atoms on GR/Ir(111); color legend: Ir, white; GR, green; and Pt, brownish (tone depending on height and layer). (d) Nominal (see text for details) and measured average clusters sizes; the latter were obtained from the distributions plotted in the bottom panel of Figure 1; data obtained from STM images.

clusters, assuming evident hexagonal shape in an extremely regular array of 60-atom particles. At the highest investigated coverage (1.5 ML), coalescence between clusters growing in adjacent cells is dominant and evident from the images, yielding large particles with on average 140 and up to 300 atoms. Comparison between 1- and 2-layer configurations has been computationally carried out for clusters of various size. In line with the experimental observations, it has been found that there is a preference for 1-layer arrangement in aggregates with $n < 20$ (Figure 2c). Considering an initially spherical Pt$_{13}$ cluster on GR/Ir(111), a simple structural optimization procedure yields a flattening of the cluster, confirming therefore the tendency of small Pt particles to wet graphene (see Figure S2 in the

Supporting Information). As a selected example of larger clusters, Pt_{31} has been simulated in a 2-layer arrangement, consisting of a first layer of 19 and a second layer of 12 atoms, as previously described.[13] At variance with the most recent calculations,[13] a full DFT optimization has been performed, which, interestingly, gives a relaxed structure that well compares with the model used to fit surface X-ray diffraction data,[13] with a strong pinning of the graphene toward the substrate (see Figure S3 in the Supporting Information).

Exposure of the former superstructures to 10 L of CO (1×10^{-7} mbar) at room temperature yields CO adsorption at the particles and mobility enhancement, thus promoting further coalescence. The filling factor decreases to almost half of the initial value for the smallest clusters, while larger particles are less influenced (Figure 2a). Consequently, the average particle size grows to 20−25 Pt atoms for the 0.05−0.25 ML coverage arrays. In Figure 3, selected STM images of the CO-covered Pt
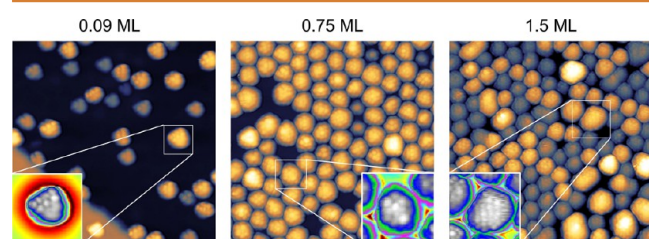

Figure 3. STM images collected at 77 K after exposure of the Pt clusters to 10 L CO at room temperature ($p_{CO} = 10^{-7}$ mbar). Insets (zoomed) show selected clusters with enhanced color contrast to highlight the CO-induced corrugation [25×25 nm^2, V_{bias} = +0.1 V, I = 50 pA].

clusters are shown for three Pt loadings. A regular structural pattern can be observed on the surface of the clusters (Figure 3, insets), showing hexagonal symmetry with a lattice constant reducing progressively from 5.0 to 4.0 Å with growing cluster size (from 0.05 to 1.5 ML Pt, respectively). On the basis of previous observations on Pt single crystal surfaces, we conclude that the pattern is associated with CO molecules adsorbed at terminal Pt sites in a $(\sqrt{3} \times \sqrt{3})$R30°-CO superstructure with a local CO coverage of 0.33 ML.[17] The DFT simulation of a 31 Pt atom cluster, structurally relaxed in the hcp adsorption region on the graphene Moiré and covered with 8 CO molecules adsorbed at Pt in on-top configuration of both the surface layer and edge sites, is reported in the top panel of Figure 4. The adsorption of CO induces a buckling in the cluster's structure and repulsive dipole interactions between the ad-molecules yield a tilt of the molecular axes, thus explaining the larger O−O distances measured on small clusters with respect to CO islands on extended (111) facets, and also in line with the observed ripening of the Cu(111) termination upon exposure to high CO pressures.[18] The agreement between the experimental and simulated STM image can be appreciated from the figure, where the CO superstructure cell is highlighted in orange. A less bright halo surrounds the clusters in the observed STM image. Interestingly, our simulated images reproduce also this feature: some molecules adsorb in bridge sites across the first and second Pt layers, pointing laterally and therefore appearing lower and darker than those adsorbed in top sites in the uppermost Pt layer and forming the brighter $(\sqrt{3} \times \sqrt{3})$R30° superstructure.

Computationally, we extensively investigated the effect of CO adsorption at nanoclusters of different size. As selected
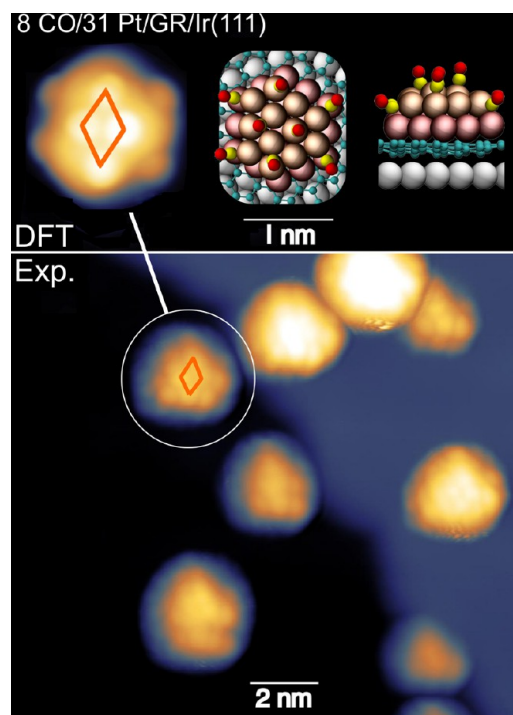

Figure 4. Comparison between experimental STM imaging of CO-covered Pt clusters (large image) and DFT simulations (upper panel, left) of a 31 atoms Pt cluster hosting 8 CO molecules. The upper panel on the right shows a model (top and side views) of the fully relaxed cluster structure, including the graphene sheet and the underlying Ir(111) terminal layer; the orange parallelograms indicate the $(\sqrt{3} \times \sqrt{3})$R30°-CO unit cell (see text for details).

examples, we show in Figure 5 the DFT optimized structures of Pt_4 (top) and Pt_{19} (bottom) clusters for increasing CO coverage (from left to right). The calculated adsorption energy E_{ads} referred to one CO molecule is also reported in Figure 5. For high CO coverage on Pt_{19}, a sizable reduction of E_{ads} is found, from 2.28 to 1.64 eV, due to intermolecular repulsion. Much smaller variations are found in case of Pt_4, from 2.00 to 2.13 eV at most, since the CO molecules have enough space to tilt and reduce their mutual repulsion. For CO adsorption on the Pt(111) single crystal surface, we obtain E_{ads} values ranging from 2.06 (zero coverage limit) down to 1.8 and 1.39 eV, in case of 0.5 and 1.0 ML (full coverage), respectively. Therefore, the presence of the GR/Ir(111) support seems to improve the affinity of Pt with respect to CO, yielding an overbinding effect. The adsorption of a single CO molecule on free-standing Pt nanoclusters has been investigated by DFT also in previous works that report E_{ads} values from 2.09 to 2.84 eV, depending on the cluster size, shape, specific adsorption site, and exchange−correlation functionals.[19,20] Our calculations for supported Pt_4 nanoclusters show that its structure is almost unaffected by CO adsorption (Figure 5, top panels). The axes of the CO molecules are not perpendicular to the surface, and for growing coverage, the CO−CO dipole repulsion increases the deviation from the normal. Pt_{19} is almost flat in absence of CO, and the adsorption of a molecule does not have relevant effects on the cluster shape, apart from a local lifting of the CO bonded Pt atoms (Figure 5, lower panels). However, the scenario changes with the adsorption of more molecules. When 12 CO molecules are adsorbed, the cluster is restructured, assuming a dome shape, with the central Pt atoms pulled up.
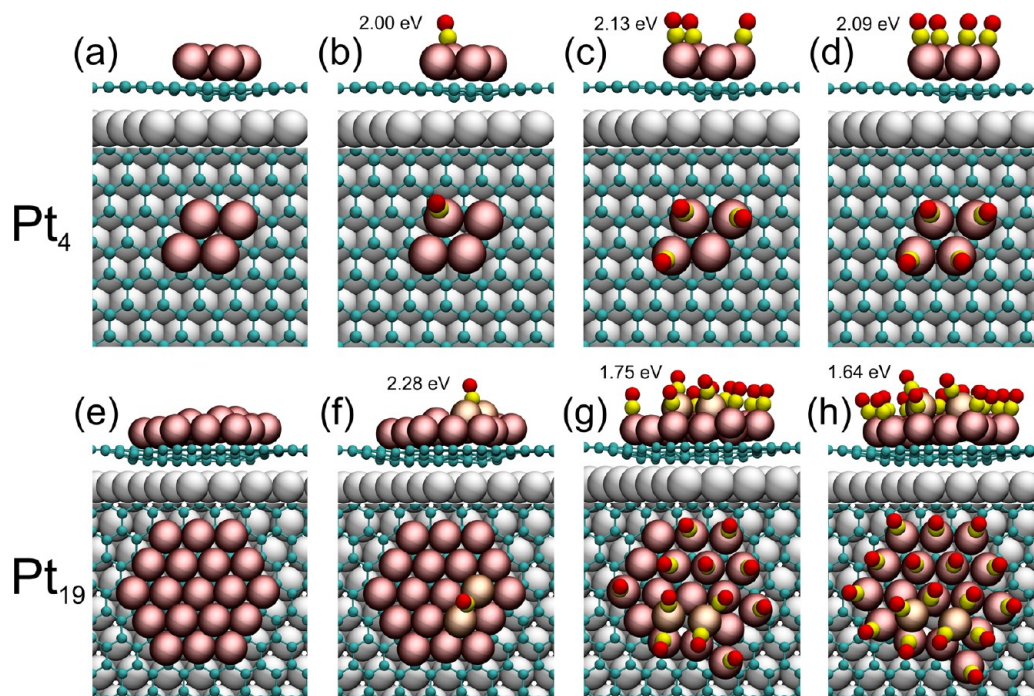
Figure 5. Fully relaxed DFT models for clusters of (a−d) 4 and (e−h) 19 atoms at increasing CO coverage (from left to right, specifically: 0, 1, 3, 4 CO on Pt₄ and 0, 1, 12, 17 CO on Pt₁₉); color legend: Ir, white; GR, green; Pt, brownish (tone depending on height); C in CO, yellow; and O in CO, red. The average CO-Pt binding energy is also reported.

The effect is even more evident with the adsorption of 17 CO molecules. The restructuring reduces the number of Pt atoms bonded to graphene, making the nanocluster−graphene interaction weaker. The strong affinity of Pt toward CO may explain the overall energy gain upon CO adsorption and reconstruction of nanoclusters, overcompensating the removal of Pt−GR bonds. As a rule of thumb, while the average strength of the Pt−GR bond is of the order of 1 eV in a flat nanocluster of 5 to 21 atoms, the average adsorption energy of CO is about twice (from 1.6 to 2.2 eV depending on the CO coverage, see Figure 5). The repulsion between the adsorbed CO molecules may induce the nanocluster restructuring, since a dome-like shape allows larger CO−CO distances and tilting with respect the adsorption on a perfectly flat Pt island. The d states of Pt and s and p orbitals of C (both in GR and from CO molecules) are mainly involved in the binding. The most significant change upon CO adsorption occurs for the d states of the Pt atoms pulled up and detached from GR, being shifted toward lower energies (see Supporting Information for further details). We can therefore argue that the mechanism described above is likely to cause an increased mobility and consequently the observed Smoluchowski ripening. The peculiar shape of restructured nanoclusters allows the adsorption of CO in different configurations, mainly in nonequivalent top sites (with Pt atoms that are either directly bound to graphene or not) and in bridge sites, as in the case of the Pt₃₁ nanoclusters with intermediate CO coverage (Figure 4, top panel). This result provides a qualitative rationale for the different peaks in SFG spectra that will be discussed in the following.

IR-vis SFG vibronic spectroscopy measurements of the C−O stretching resonance were performed *in situ* upon exposure of the ordered Pt clusters at room temperature to CO pressures progressively increasing from 10^{-8} to 1 mbar. Figure 6 displays the SFG data together with the best fit and the deconvolution of the resonances according to the procedure described in the

Methods section. Four nonequivalent stretching modes (P_i, $i = 1-4$), corresponding to CO molecules adsorbed in nonequivalent sites, are observed, depending on the adsorption conditions. Two vibrational features are observed for the lowest Pt coverage (0.05 ML) in 10^{-8} mbar CO: P_2 at $\omega_2 = 1975$ (green) and P_3 at $\omega_3 = 2039$ cm^{-1} (violet), blue-shifting with increasing pressure up to 2000 and 2071 cm^{-1}, respectively. At first glance, a single broad and dispersive spectral feature may be used for the best fit of the observed SFG intensity modulation. However, it is found that two features are necessary to accurately reproduce the experimental data, thus confirming the presence of two distinct contributions. In addition, a third peak, P_1 (yellow), with very low intensity and dispersive line shape is observed at $\omega_1 = 1845$ cm^{-1}. A significant Gaussian broadening of the whole spectrum is also found ($\sigma = 25$ cm^{-1}), suggesting a consistent structural and chemical inhomogeneity, in agreement with the STM measurements. A similar situation is observed also for 0.09 ML Pt, with $\omega_1 = 1871$ cm^{-1}, $\omega_2 = 1969-1993$ cm^{-1}, and $\omega_3 = 2041-2057$ cm^{-1}, respectively, while the Gaussian broadening reduces to $\sigma = 15$ cm^{-1}. At 0.25 ML Pt, a fourth feature P_4 (red) appears in the $\omega_4 = 2076-2087$ cm^{-1} range, depending on the CO pressure, and the inhomogeneity contribution further decreases to $\sigma = 11$ cm^{-1}. The intensity of the fourth resonance increases by almost 1 order of magnitude when further increasing the Pt cluster size up to 1.5 ML, while no additional features appear. As a general trend, the line shape analysis of the IR-vis SFG signal reveals a relevant weakening of the observed Gaussian broadening, from 25 down to 7 cm^{-1}, for increasing Pt loading (see Figure S4, left, in the Supporting Information). This is in agreement with the STM images that show an increased degree of order of the superlattice for larger particles. In addition, higher CO pressures yield a typical, progressive blue-shift of the stretching features (see Figure S5), consistent with a denser CO phase at the clusters' surface and with the CO-induced
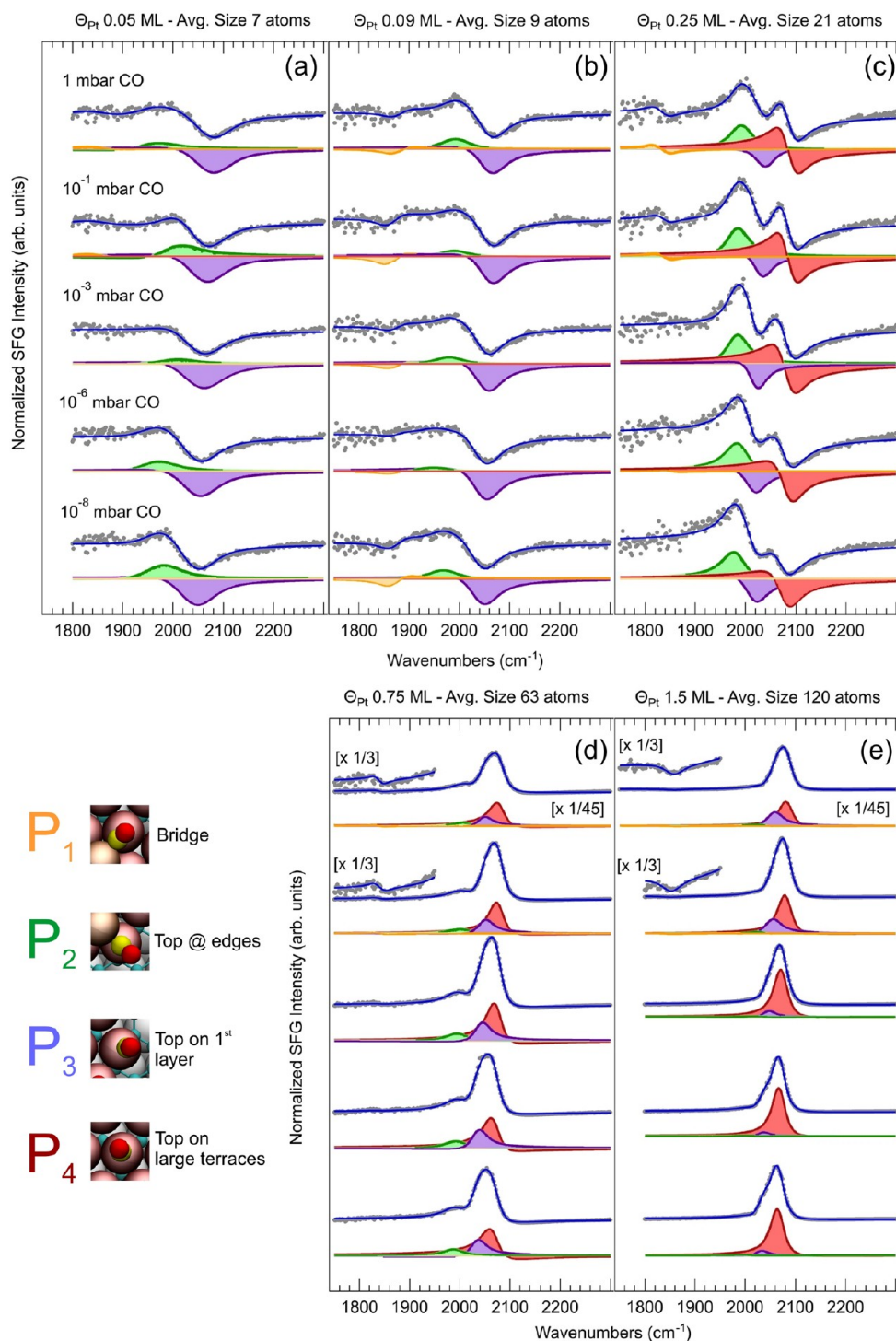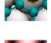
Figure 6. IR-vis SFG spectra in the C−O stretching region collected at room temperature *in situ* for increasing Pt cluster size (from a to e) and for increasing CO pressure (from bottom to top in each of the panels) spanning from UHV to NAP conditions. Data (gray dots) and the results of the least-squares fitting (blue lines) are shown. Color-filled curves represent deconvoluted intensity modulations with respect to the nonresonant background (see text for further details). The labeling and color mapping of the deconvolution are shown in the bottom left part of the figure, together with pictorial models for the nonequivalent CO adsorption sites [λ_{Vis} = 532 nm; ppp polarization].

coalescence of adjacent particles. The values of the best fitting parameters of the data plotted in Figure 6 are reported in the Supporting Information (Tables S1−S5), while the line positions and the assignment of the SFG resonances are reported in Table 1. The position of the resonances can provide precious information about the strength of the CO bonding to the metal and thus about the adsorption site. Upon adsorption

on Pt, the C−O stretching frequency is red-shifted with respect to the gas-phase value, due to the weakening of the C−O molecular bond. This is readily understood on the basis of the bonding mechanism, well described within the framework of the Blyholder model.[21−23] The hybridized states between CO and Pt originate from the σ electron donation from the 5σ orbital of CO to the vacant 6sp conduction band of Pt and from

Table 1. Positions of the C−O Stretching Resonances Together with Literature Referencing and Proposed Assignment[a]

Resonance	Energy (cm^{-1})	Reference (cm^{-1})	Assignment (adsorption site)	
P$_1$	1840-1870	1845-1855[24,25,29]	Pt − bridge	
P$_2$	1980-2010	2000[22]	Pt − top @ edge, corners	
P$_3$	2015-2060	2065-2078[27,28]	Pt − top @ borders, 1st layer terraces	
P$_4$	2060-2090	2072-2104[17,24−30]	Pt − top @ terraces of large clusters	
P$_5$	2040-2057	2063-2079[36,59]	Ir − top, intercalated under graphene	
P$_6$	1880	-	Pt − bridge	

[a]Models of the adsorption sites are depicted in the last column and are intended as exemplificative only.
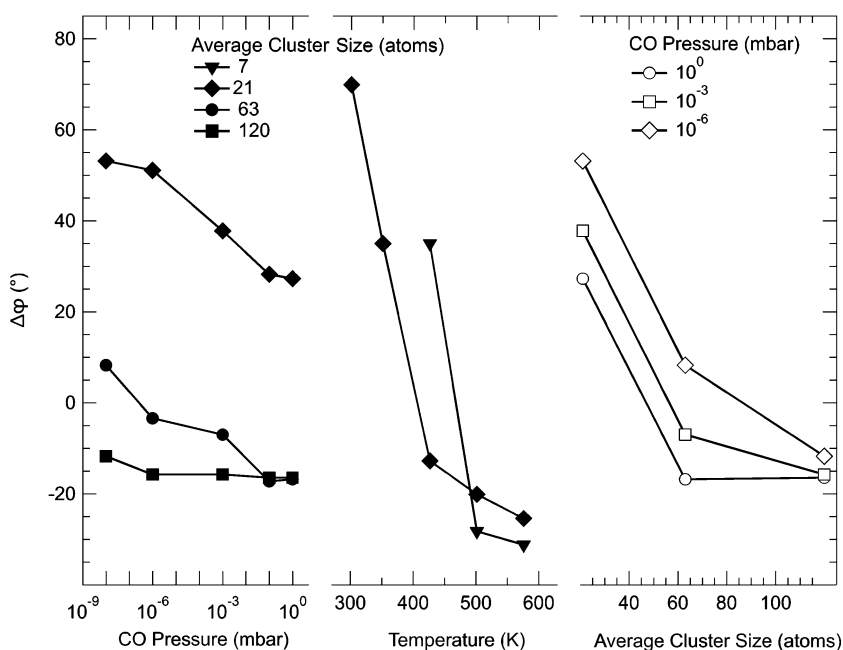

Figure 7. Phase of the IR-vis SFG C−O stretching resonances with respect to the nonresonant background for different cluster sizes as a function of CO pressure at room temperature (left), sample temperature in 0.1 mbar CO (center), and as a function of the cluster size at different CO pressures (right).

the π back-donation from the 5d of Pt to the vacant antibonding $2\pi^*$ orbital of CO. The latter is mainly responsible for the weakening of the C−O bond and hence the red-shift with respect to the resonance at 2170 cm^{-1} of free CO.[21] In the case of adsorption on Pt, a simple model can be obtained by considering the coordination number. The lower the Pt coordination number, the stronger the Pt−CO interaction, thus the stronger the electron back-donation and the weaker the C−O bond.[22] On the basis of the above considerations and with reference to established literature, we then attribute the highest energy feature P$_4$ to CO molecules adsorbed on top of Pt atoms in the middle of (111) terraces on multilayer clusters (Pt−Pt coordination 9).[24−29] Indeed, P$_4$ grows for Pt loadings higher than 0.25 ML, when 2-layer clusters start growing. Consequently, we associate P$_3$ with CO at on top Pt sites of (111) terraces of single-layer clusters (Pt−Pt coordination 6) at 0.05 and 0.09 ML Pt coverage. For thicker clusters, we attribute this feature to CO adsorbed on top of edge Pt atoms at the borders of the first layer of the cluster (Pt−Pt coordination

number 7).[26−28] P$_2$ instead gives a negligible contribution to SFG spectra from small clusters, while its intensity grows for higher Pt loadings. By applying the same reasoning, we conclude that it is due to CO molecules on top of the edge Pt atoms on single-layer clusters and of corner atoms on multilayer clusters (Pt−Pt coordination 4 and 3).[22] Lastly, P$_1$ is the lowest energy feature that we observe, almost exclusively for high CO pressures and with growing intensity for larger cluster sizes. Under high CO coverage conditions (>0.5 ML), CO adsorbs on (111) terraces forming a $c(4 \times 2)$ super-structure, so that bridge sites also get populated.[17,26,29] For CO adsorbed in this configuration, both the IR and Raman cross sections are smaller, thus explaining the lower intensity with respect to molecules at terminal Pt sites.[29] We therefore attribute P$_1$ to CO molecules at bridge Pt sites. The population of differently coordinated sites was observed by means of XPS also in the case of CO adsorption at low temperature under UHV conditions on Pt clusters grown on GR/Rh(111),[12] thus further supporting our assignments. In our SFG spectra, we

observe that the positions of the vibrational features associated with on top CO experience a monotonous blue-shift for increasing CO pressure (Figure S5 in the Supporting Information), similar to the case of CO adsorption on a Pt(111) surface,[17,30] due to dipole–dipole coupling between adjacent molecules. In parallel, progressively larger (111) facets associated with CO-induced ripening of the clusters[10] yield a more homogeneous system and smaller Gaussian contributions to the spectral inhomogeneity broadening (Figure S4, left, in the Supporting Information). From the fitting procedure, the phase of the resonances with respect to the nonresonant background can also be obtained. As mentioned in the Methods section, in homodyne SFG, the identification of the line shape parameters is not unique, but once a first set of parameters is obtained, the $2^{N-1} - 1$ remaining sets can be mathematically extracted in a straightforward way.[31] In Figure 7, we therefore plot the relative phase φ_4 as a function of the system and adsorption pressure and φ_4 together with φ_5 as a function of the temperature (details in the following). As it can be directly observed also by eye when looking at the raw SFG spectra, we measure a clockwise rotation of the phase for increasing CO pressure, temperature, and cluster size, thus with the progressive formation of larger (111) Pt facets. If we exclude geometric contributions due to a change in the average orientation of the CO dipole, this effect may by associated with the electronic transition that is involved in the resonant SFG vibronic process. This issue has already been investigated by means of doubly resonant SFG spectroscopy on the CO/Pt(111) system,[21] and the charge-transfer state associated with the C–O stretching mode was found to be at 2.51 eV, with a bandwidth of 0.83 eV, thus close to and compatible with our visible beam excitation (532 nm, 2.33 eV). The resonance involves the transition from the 5d to the 6sp orbital of Pt hybridized with the 5σ orbital of CO. Therefore, changes in the Pt electronic configuration due to cluster restructuring may be indirectly reflected in the apparent resonance's phase. The latter may be interpreted as a spectroscopic fingerprint of the dispersion and ripening of the clusters' superlattice when CO is exploited as a probe molecule. The influence of finite-size effects on the SFG signal, in relation with the interference of the resonant and nonresonant contributions, was already observed for CO adsorption on palladium clusters.[32,33] In particular, in that case, by changing the visible beam wavelength and thus by moving the excitation energy with respect to the electronic resonance, a consistent relative phase change was measured. Here, by changing the clusters' size, instead of changing the photon, we change the energy of the system's plasmonic resonance.[34]

When heating the system above room temperature in 0.1 mbar CO, several changes are observed in the SFG spectra. In Figure 8 we plot the C–O stretching region measured in the 300–575 K range for 0.05 (left) and 0.25 ML (right) of Pt on graphene. Starting from 425 K, the P_4 component (red) is replaced by P_5 (light red), with a noticeable phase change and with a burst in amplitude (notice that the spectra at 500 and 575 K have been divided by two in order to fit into the panel), showing a red-shift of about 50 cm^{-1} down to the 2040–2057 cm^{-1} range, depending on the conditions. While the phase shift mostly occurs at low temperature (Figure 7, central panel), the red-shift of the peak is more gradual with temperature. The first effect can be ascribed to a change in the electronic structure of the adsorption site, compatible with the spillover of CO from the Pt clusters to the Ir surface, while the red-shift is associated
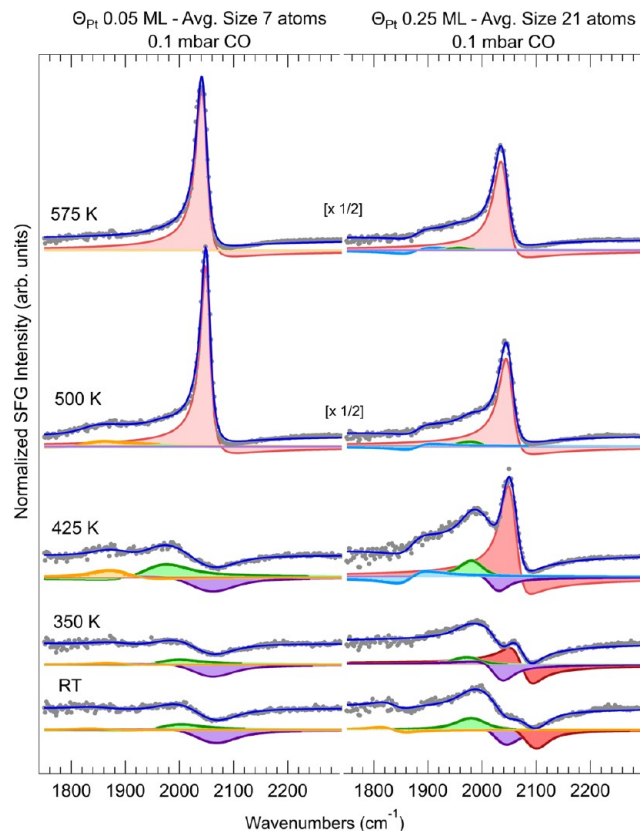

Figure 8. IR-vis SFG spectra in the C–O stretching region collected *in situ* at 0.1 mbar CO as a function of the sample temperature for 0.05 ML (left) and 0.25 ML Pt (right), respectively [λ_{Vis} = 532 nm; ppp polarization].

with temperature-related anharmonic coupling with the CO frustrated translation modes,[35] as already observed for CO/Ir(111), where the C–O stretching mode is observed in the 2063–2079 cm^{-1} interval,[36] close to the values we find here. The intensity burst of P_5 may instead be associated with the progressive growth of densely packed CO islands at the Ir(111) surface, as observed in the case of CO intercalation at the GR/Ir interface.[37] CO adsorption on Pt (111) islands at near-ambient pressure conditions would instead yield a sharp resonance at about 2100 cm^{-1}, thus at higher energy.[15,24] In parallel, in the case of the large clusters, a new and broader component (P_6, cyan) grows at about 1880 cm^{-1}, most probably associated with thermal induced loss of registry and inhomogeneity of CO in bridge Pt sites.[24] In order to better understand the observed behavior, we also collected NAP-XPS spectra. In Figure 9 we plot the C 1s (a and b) and Pt $4f_{7/2}$ regions (c) measured at room temperature (bottom) and at 420 K (top) in 0.1 mbar CO on the bare graphene (a) and on the 0.25 ML Pt on graphene systems (b and c). In the former case, no CO adsorption occurs, and there is no evident change upon heating in the C 1s line shape at 284.1 eV associated with graphene, apart from an increased Gaussian broadening due to thermal effects. No C–O stretching features are observed in the SFG spectra either. Since CO does not stick on graphene, this indicates that a perfect and complete graphene single layer was grown and that no CO intercalation occurred. Indeed, when the graphene sheet is defective or incomplete, small molecules like CO and O_2 have been observed to intercalate and adsorb at the underlying Ir(111) surface at near-ambient pressure con-
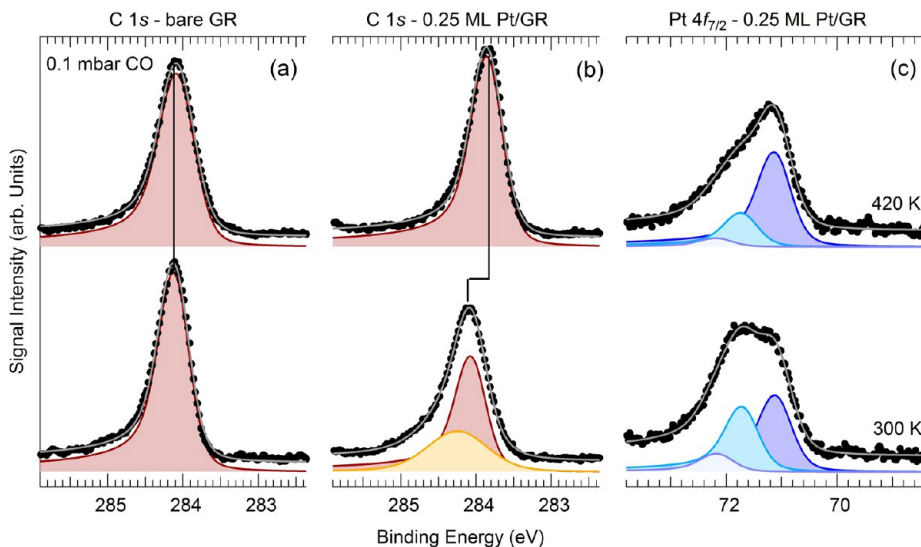
Figure 9. NAP-XPS spectra in 0.1 mbar CO collected at room temperature (bottom) and at 420 K (top): C 1s region (a) from the bare graphene sheet on Ir(111); and C 1s (b) and Pt $4f_{7/2}$ (c) regions of Pt clusters (0.25 ML Pt on graphene) [$h\nu$ = 1486.6 eV, PE = 10 eV].

ditions.[37,38] When the Pt clusters are present (Figure 9b, bottom), instead, a broad rehybridization shoulder appears in the C 1s spectrum at higher binding energy (yellow peak), at the expense of the intensity of the peak at 284.1 eV. This is in remarkable agreement with CO adsorption on the same system under UHV conditions.[14] The broad feature is attributed to the nonequivalent sp³ C atoms of graphene in between the Pt clusters and the underlying iridium surface.[10,11,13,14] Upon heating, we observe a −0.3 eV shift of the main graphene component (284.1 eV) to lower binding energy (283.8 eV), while the high binding energy feature is not visible any more (the best fitting parameters are reported in Table S8 in the Supporting Information). A shift of −0.3 eV of the graphene C 1s peak has already been observed at near-ambient pressure in the case of intercalation of CO between the graphene and the Ir(111) surface, where the $(3\sqrt{3} \times 3\sqrt{3})R30°$-CO/Ir(111) superstructure is formed.[37,39] We thus conclude that, upon annealing, Pt catalyzes the intercalation of CO to the underlying metal surface. Consistently, we find that the C 1s feature at 286.3 eV associated with CO (see Figure S6 in the Supporting Information) grows in intensity upon annealing from room temperature to 420 K. Pt $4f_{7/2}$ core level spectra collected *in situ* provide further insight (Figure 9c). It is already known that the geometric and chemical inhomogeneity of Pt atoms combined in a small cluster structure show a progression of different Pt 4f chemical shifts.[11] Indeed, while Pt ad-islands on the bare Ir(111) surface yield a single sharp contribution at 70.88 eV, in the case of a single layer 19 Pt atom cluster on the graphene sheet, the spectrum spans 1 eV in binding energy, with a principal contribution at about 70.8 eV. Adsorption of CO on a nanostructured Pt surface at 10^{-1} mbar was found to induce, besides the bulk Pt $4f_{7/2}$ component at 71.10 eV, the growth of two spectroscopic features shifted by +0.60 and +1.05 eV, associated with terrace and low-coordinated Pt atoms bound to CO.[16] A similar upshift of the Pt core level binding energy upon adsorption of CO was already observed on our same system under UHV conditions.[14] As shown in Figure 9c, the same components as in the case of the stepped Pt surface were successfully used to deconvolve our Pt spectra (the fitting parameters are reported in Table S9 in the Supporting Information). It is important to note that the higher binding

energy components were found to grow in intensity with increasing CO pressure from 10^{-9} to 10^{-1} mbar in the case of CO-induced rippling of a single crystal Pt surface, yielding nanometer-sized clusters.[16] In the present case of Pt clusters on the GR/Ir(111) template, upon annealing we observe a decrease in the intensity of the core level shifted components, compatible with a cluster coalescence process. It has indeed already been shown, in the case of Rh clusters grown on the same support,[40] that a bulk-related metal core level component is already observable for clusters of 60−80 atoms and accounts for about 50% of the signal after temperature-induced coalescence of 0.37 ML Rh clusters, thus supporting our assignment of the 71.10 eV feature to bulk-coordinated Pt atoms. The mechanism for CO intercalation is unexplained yet: the increased intensity of the Pt $4f_{7/2}$ component at 71.10 eV at the expense of the CO-induced features is compatible with the formation of larger Pt agglomerates, while the graphene network is catalytically opened to allow CO spillover to the GR/Ir(111) interface. Remarkably, previous STM investigations have demonstrated that Pt clusters (0.25 ML Pt) are stable on GR/Ir(111) up to 400 K, whereas coalescence sets in for higher temperature.[8] Cycles of CO adsorption at room temperature followed by oxidation at 575 K on this system under UHV conditions (10^{-7} mbar) have shown that the Pt clusters undergo reversible shape changes, with a decreased radius and increased thickness in the presence of CO with respect to the clean system, in a breathing-like cycle.[13] In any case, no degradation of the underlying graphene sheet has been observed under these vacuum conditions, at variance with our near-ambient pressure experiments where Pt particles promote diffusion of CO under the graphene sheet. Temperature-induced cluster intercalation has been observed for strong interacting graphene systems like GR on Ru, Ni, and Rh, but to our knowledge, this was not observed at the Ir surface, even if a possible role of gas-phase reactants was suggested.[7] In the present case, we observe the disappearance of the high binding energy feature in the C 1s XPS spectrum of GR at 420 K (Figure 9b), possibly indicating that the sp³ C atoms at the Pt−Ir interface are not present any more or at least are reduced in number. This may be a further confirmation that the CO−Pt interaction is stronger than the Pt−GR interaction; the latter

being further weakened upon adsorption of CO, similarly to what was proposed under UHV conditions.[14] Alternatively, it may also be compatible with the intercalation of the Pt clusters under GR, but further investigations are necessary to confirm this latter interpretation.

CONCLUSIONS

We studied the adsorption of CO from UHV to near-ambient pressure on a regular array of Pt nanoclusters supported by graphene/Ir(111). By means of a combination of experimental techniques (*in situ* nonlinear photon in−photon out spectroscopy, photon in−electron out spectroscopy, and microscopy) and numerical simulations based on *ab initio* methods, we find that both terminally and bridge bonded CO species populate nonequivalent sites of the clusters, spanning from first to second-layer terraces to borders and edges, depending on the particle size and morphology and on the adsorption conditions. A significant restructuring of the clusters is observed upon CO adsorption at room temperature, promoting particle sintering for small clusters and reshaping for large ones. In the latter case, Pt atoms in the center of the cluster are lifted upon binding with CO, and a progressively lower Pt−Pt coordination is observed for increasing CO coverage. Above room temperature, Pt clusters catalyze the spillover of CO at 0.1 mbar to the underlying graphene/Ir(111) interface.

METHODS

Experimental Section. IR-vis sum frequency generation vibronic spectroscopy measurements were performed in a dedicated setup at the Physics Department of the University of Trieste. A detailed description of the system can be found elsewhere.[36] A high-pressure reactor is directly connected to an UHV system with a base pressure of 5×10^{-11} mbar, hosting standard techniques for surface preparation and characterization. The reactor is equipped with a gas handling system to control the CO pressure in the $10^{-9}-10^{+1}$ mbar range. CO was dosed from aluminum bottles through aluminum piping and brass valves in order to avoid carbonyl contaminations. The inlet of the infrared and visible beams, as well as the outlet of the SFG signal, are provided by UHV-compatible BaF_2 windows. The Ir(111) disc was mounted and resistively heated by means of Ta wires. The excitation source (EKSPLA) delivers a 532 nm visible beam and tunable IR radiation in the $1000-4500$ cm^{-1} range yielding, together with the detection system, an ultimate energy resolution better than 6 cm^{-1}. After normalization to the IR and visible excitation intensities, the SFG spectra were analyzed by least-squares fitting to a parametric, effective expression of the nonlinear second-order susceptibility.[31,36,41−44] The expression (reported in the following) reproduces the observed lineshapes, accounting for the resonant IR-vis vibronic transitions and for the nonresonant background, and describing all the interference terms:

$$\frac{I_{\text{SFG}}(\omega_{\text{IR}})}{I_{\text{vis}}I_{\text{IR}}(\omega_{\text{IR}})} \propto \left| A_{\text{NRes}} + \sum_k \frac{A_k e^{i\Delta\varphi_k}}{\omega_{\text{IR}} - \omega_k + i\Gamma_k} \right|^2$$

where A_{NRes} and A_k account for the amplitudes of the nonresonant and k_{th}-resonant contributions, respectively, $\Delta\varphi_k$ is the phase difference between the k_{th}-resonant and nonresonant signals, ω_k is the energy position of the line, and Γ_k its Lorentzian broadening that is related to the dephasing rate, which in turn stems from the energy lifetime and from the elastic dephasing of the excited vibronic state.[45] In order to account for inhomogeneity broadening, the line shape was also convoluted with a Gaussian envelope.[36,46−48] A best-fitting set of parameters is known to be nonunique in homodyne SFG, since 2^{N-1} equivalent sets can be obtained when N resonances are present in the spectrum. However, once an optimal set is extracted from the data by least-squares fitting, the remaining equivalent sets can be easily obtained mathematically.[31] In the manuscript's figures, we plot the normalized SFG signal intensity (gray dots) together with the best fit (blue lines). We also plot (color-filled curves) the intensity of each resonance and its interference with the nonresonant background by calculating, with the parameters obtained from the fitting procedure, the following quantity:

$$\frac{I_{\text{SFG},k}(\omega_{\text{IR}})}{I_{\text{vis}}I_{\text{IR}}(\omega_{\text{IR}})} \propto \left| A_{\text{NRes}} + \frac{A_k e^{i\Delta\varphi_k}}{\omega_{\text{IR}} - \omega_k + i\Gamma_k} \right|^2$$

These plots directly put in evidence the amplitude and the relative phase for each of the resonances. Further details can be found in our previous work.[36] In the present study, all spectra were collected in the ppp polarization configuration (SFG-vis-IR).

Low-temperature scanning tunneling microscopy (LT-STM) measurements were carried out at 77 K with an Omicron LT-STM system. The microscope is hosted in a UHV chamber, operating at a base pressure of 1×10^{-10} mbar. Images were collected in constant current mode, with the bias applied to the sample and a grounded W tip. STM images were analyzed by subtracting a background plane to correct the sample tilting and by applying an appropriate affine transformation to calibrate the lateral scale and compensate for thermal drift effects.

Near-ambient pressure X-ray photoelectron spectroscopy (NAP-XPS) measurements were performed in a commercial setup (SPECS Surface Nano Analysis GmbH) at the Surface Science Laboratory of the Charles University in Prague. Spectra were collected by means of a Phoibos 150 hemispherical electron energy analyzer coupled with a differentially pumped electrostatic prelens system. The reaction cell is installed in the analysis chamber with a chamber-in-chamber design. Monochromatized Al K$_\alpha$ radiation (1486.6 eV) was employed. All spectra were collected with a pass energy of 10 eV. After normalization to the low binding energy background, spectra were analyzed by least-squares fitting of the data with Doniach−Šunjić profiles,[49] convoluted with a Gaussian envelope to account for experimental resolution, inhomogeneity, and thermal broadening. A linear background was also accounted for. Binding energies were calibrated using the Ir 3d$_{5/2}$ core level as reference. A carbonyl cold trap was exploited to purify CO.

In all cases, the Ir(111) single crystal (Mateck) was cleaned by standard cycles of Ar$^+$/Ne$^+$ sputtering and annealing in UHV, alternated with oxygen treatments. Temperature was measured by means of a K-type thermocouple. Graphene was grown by thermal cracking of ethylene dosed from the background in vacuum, following established recipes.[50] In detail, after saturation with ethylene at room temperature, the crystal was annealed to 1100 K. At 1100 K, an ethylene background was introduced, and the temperature was further increased up to 1300 K. A temperature cycle (1300−500−1300 K) followed, always in ethylene background. The complete GR growth treatment lasted 40 min. Platinum clusters were obtained by self-assembly at room temperature upon physical vapor deposition from the gas phase.[8,13,51] Pt atoms were evaporated from a 0.2 mm diameter, pure Pt wire that was resistively heated. Depending on the setup, a precise quantification of the Pt coverage was obtained by (i) calibration of the evaporator by means of a quartz micro balance (SFG), (ii) the C 1s, Pt 4f, and Ir 3d core level intensities (XPS), and (iii) a local calibration by means of imaging of Pt/Ir(111) ad-islands (STM). The three methods yielded different Pt coverage calibration accuracies, of the order of 10, 30, and 5%, respectively.

Theoretical. Quantum mechanical simulations were carried out in the framework of DFT, using the Quantum ESPRESSO code,[52] with the generalized gradient approximation for the exchange−correlation functional in the Perdew, Burke, and Ernzernhof parametrization (GGA-PBE) using ultrasoft pseudopotentials.[53] Semiempirical corrections accounting for the van der Waals interactions, that have been proved important to properly describe the binding of epitaxial graphene with transition metals, are included with the DFT-D approach.[54] After convergence tests, we set a kinetic energy cutoff of 30 Ry for wave functions and of 300 Ry for the charge density basis sets, and we used the Methfessel−Paxton smearing technique, with an energy broadening of 0.02 Ry.[55] The calculated equilibrium lattice

parameters are 2.46 and 2.75 Å for graphene and for the Ir(111) surface, respectively, in excellent agreement with previous works[51] and with the experimental values of 2.46 and 2.715 Å, respectively (the latter derived from the bulk value).[56] The Moiré structure of GR/Ir(111) is modeled using a supercell with 10 × 10 GR unit cells on 9 × 9 Ir surface (111) unit cells, with the in-plane parameter fixed at the Ir value. The graphene layer is therefore stretched by only 0.6% with respect to its equilibrium lattice constant. To reduce the computational effort, the Ir substrate is modeled with a 2-layer slab geometry, for a total of 362 atoms included in the simulations. The repeated slabs are separated by about 26 Å, a space large enough to accommodate also the presence of clusters without introducing fictitious interactions with repeated images. Γ-point sampling is used for Brillouin zone integration. The interplanar distance between the terminal and second Ir layers is 2.15 Å, kept fixed and derived from a full optimization of a 1 × 1 Ir(111) slab. The position of the graphene layer is also optimized: in the absence of Pt, the result is an almost flat layer, with an average distance from the substrate of 3.13 Å and a corrugation of about 0.3 Å. The registry of the graphene layer with the substrate changes with continuity in the different regions of the supercell. It can be characterized by the relative position of the center of the hexagons of graphene with respect to the Ir atoms of the substrate, as already proposed in several previous works. In this way, fcc, hcp, and atop regions can be identified, which correspond to hcp-top, fcc-top, and fcc-hcp positions of the carbon atoms, respectively.[56] Fcc and hcp regions are the closest to the substrate, with a distance of 3.00 Å, whereas the atop region is the most distant (3.25 Å). The model details are reported in Figure S1 of the Supporting Information. Since Pt deposition affects the graphene structure, with pinning effects depending on the Pt loading, the graphene geometry is optimized in each run.

For a series of calculations regarding small nanoclusters of various sizes (up to 9 atoms) adsorbed in different regions of the Moiré structure and on different sites, we used reduced models to limit the computational workload. In this view, we performed calculations in a supercell with 5 × 5 GR unit cells stretched to match 5 × 5 Ir(111) surface cells (see Figure S1, panel b); three different models have been used, considering different registries between graphene and the substrate in order to mimic the nonequivalent fcc, hcp, and atop regions. For the reduced models, a 3-layer slab of Ir has been always used. We checked that the results do not change significantly if only 2 layers are considered, therefore validating that choice for the full model. The Brillouin zone was sampled using a 2 × 2 × 1 Monkhorst−Pack grid,[57] centered at the Γ-point. For symmetry reasons, in the reduced models, the epitaxial graphene without adsorbed nanoclusters is perfectly flat, with a distance from the substrate which is very close to the one obtained in the more realistic, larger model. Even though the size constrains introduced in the reduced models limit the possibility of deformation of graphene upon nanocluster adsorption, some tests with the larger model confirm the trends obtained.

In order to simulate STM images, we use the Tersoff−Hamman approach,[58] according to which the tunneling current is proportional to the energy-integrated electronic local density of states (ILDOS). Specifically, in order to better mimic the experimental STM images acquired in a constant-current mode, we map an ILDOS iso-surface instead of doing the conventional section on a plane parallel to the surface that simulates a constant-height mode.

ASSOCIATED CONTENT

ⓢ Supporting Information

The Supporting Information is available free of charge on the ACS Publications website at DOI: 10.1021/acsnano.6b07876.

> DFT models of the GR/Ir(111) system and structural models for Pt/GR/Ir(111); SFG Gaussian broadening parameters, blue-shifts of the resonances, DOS from DFT, and tables of the SFG and XPS best fitting parameters according to the line shape described in the text (PDF)

AUTHOR INFORMATION

Corresponding Author

*vesselli@iom.cnr.it.

ORCID ⊕

Carlo Dri: 0000-0001-9040-5746

Erik Vesselli: 0000-0002-6799-0032

Notes

The authors declare no competing financial interest.

REFERENCES

(1) Vajda, S.; Pellin, M. J.; Greeley, J. P.; Marshall, C. L.; Curtiss, L. A.; Ballentine, G. A.; Elam, J. W.; Catillon-Mucherie, S.; Redfern, P. C.; Mehmood, F.; et al. Subnanometre Platinum Clusters as Highly Active and Selective Catalysts for the Oxidative Dehydrogenation of Propane. *Nat. Mater.* 2009, 8, 213−216.

(2) Valden, M. Onset of Catalytic Activity of Gold Clusters on Titania with the Appearance of Nonmetallic Properties. *Science* 1998, 281, 1647−1650.

(3) Stephens, I. E. L.; Elias, J. S.; Shao-Horn, Y. The Importance of Being Together. *Science* 2015, 350, 164−165.

(4) Calle-Vallejo, F.; Tymoczko, J.; Colic, V.; Vu, Q. H.; Pohl, M. D.; Morgenstern, K.; Loffreda, D.; Sautet, P.; Schuhmann, W.; Bandarenka, A. S. Finding Optimal Surface Sites on Heterogeneous Catalysts by Counting Nearest Neighbors. *Science* 2015, 350, 185−189.

(5) Ding, K.; Gulec, A.; Johnson, A. M.; Schweitzer, N. M.; Stucky, G. D.; Marks, L. D.; Stair, P. C. Identification of Active Sites in CO Oxidation and Water-Gas Shift over Supported Pt Catalysts. *Science* 2015, 350, 189−192.

(6) Tyo, E. C.; Vajda, S. Catalysis by Clusters with Precise Numbers of Atoms. *Nat. Nanotechnol.* 2015, 10, 577−588.

(7) Henry, C. R. 2D-Arrays of Nanoparticles as Model Catalysts. *Catal. Lett.* 2015, 145, 731−749.

(8) N'Diaye, A. T.; Gerber, T.; Busse, C.; Myslivecek, J.; Coraux, J.; Michely, T. A Versatile Fabrication Method for Cluster Superlattices. *New J. Phys.* 2009, 11, 103045.

(9) Linas, S.; Jean, F.; Zhou, T.; Albin, C.; Renaud, G.; Bardotti, L.; Tournus, F. Moiré Induced Organization of Size-Selected Pt Clusters Soft Landed on Epitaxial Graphene. *Sci. Rep.* 2015, 5, 13053.

(10) Gerber, T.; Knudsen, J.; Feibelman, P. J.; Grånäs, E.; Stratmann, P.; Schulte, K.; Andersen, J. N.; Michely, T. CO-Induced Smoluchowski Ripening of Pt Cluster Arrays on the Graphene/Ir(111) Moiré. *ACS Nano* 2013, 7, 2020−2031.

(11) Knudsen, J.; Feibelman, P. J.; Gerber, T.; Grånäs, E.; Schulte, K.; Stratmann, P.; Andersen, J. N.; Michely, T. Clusters Binding to the Graphene Moiré on Ir(111): X-Ray Photoemission Compared to Density Functional Calculations. *Phys. Rev. B: Condens. Matter Mater. Phys.* 2012, 85, 35407.

(12) Gotterbarm, K.; Späth, F.; Bauer, U.; Bronnbauer, C.; Steinrück, H.-P.; Papp, C. Reactivity of Graphene-Supported Pt Nanocluster Arrays. *ACS Catal.* **2015**, *5*, 2397−2403.

(13) Franz, D.; Blanc, N.; Coraux, J.; Renaud, G.; Runte, S.; Gerber, T.; Busse, C.; Michely, T.; Feibelman, P. J.; Hejral, U.; et al. Atomic Structure of Pt Nanoclusters Supported by graphene/Ir(111) and Reversible Transformation under CO Exposure. *Phys. Rev. B: Condens. Matter Mater. Phys.* **2016**, *93*, 45426.

(14) Gerber, T.; Grånäs, E.; Schröder, U. A.; Stratmann, P.; Schulte, K.; Andersen, J. N.; Knudsen, J.; Michely, T. Stability and Reactivity of Graphene-Templated Nanoclusters. *J. Phys. Chem. C* **2016**, *120*, 26290−26299.

(15) Rupprechter, G.; Dellwig, T.; Unterhalt, H.; Freund, H.-J. High-Pressure Carbon Monoxide Adsorption on Pt(111) Revisited: A Sum Frequency Generation Study. *J. Phys. Chem. B* **2001**, *105*, 3797−3802.

(16) Tao, F.; Dag, S.; Wang, L.-W.; Liu, Z.; Butcher, D. R.; Bluhm, H.; Salmeron, M.; Somorjai, G. a. Break-Up of Stepped Platinum Catalyst Surfaces by High CO Coverage. *Science* **2010**, *327*, 850−853.

(17) Crossley, A.; King, D. A. Infrared Spectra for Co Isotopes Chemisorbed on Pt(111): Evidence for Strong Absorbate Coupling Interactions. *Surf. Sci.* **1977**, *68*, 528−538.

(18) Eren, B.; Zherebetskyy, D.; Patera, L. L.; Wu, C. H.; Bluhm, H.; Africh, C.; Wang, L.-W.; Somorjai, G. A.; Salmeron, M. Activation of Cu(111) Surface by Decomposition into Nanoclusters Driven by CO Adsorption. *Science* **2016**, *351*, 475−478.

(19) Davis, J. B. A.; Baletto, F.; Johnston, R. L. The Effect of Dispersion Correction on the Adsorption of CO on Metallic Nanoparticles. *J. Phys. Chem. A* **2015**, *119*, 9703−9709.

(20) Figueiredo, M. C.; Melander, M.; Solla-Gullón, J.; Kallio, T.; Laasonen, K. Bismuth and CO Coadsorption on Platinum Nanoparticles. *J. Phys. Chem. C* **2014**, *118*, 23100−23110.

(21) Chou, K. C.; Westerberg, S.; Shen, Y. R.; Ross, P. N.; Somorjai, G. A. Probing the Charge-Transfer State of CO on Pt(111) by Two-Dimensional Infrared-Visible Sum Frequency Generation Spectroscopy. *Phys. Rev. B: Condens. Matter Mater. Phys.* **2004**, *69*, 153413.

(22) Kappers, M. J.; van der Maas, J. H. Correlation between CO Frequency and Pt Coordination Number. A DRIFT Study on Supported Pt Catalysts. *Catal. Lett.* **1991**, *10*, 365−373.

(23) Aizawa, H.; Tsuneyuki, S. First-Principles Study of CO Bonding to Pt(111): Validity of the Blyholder Model. *Surf. Sci.* **1998**, *399*, L364−L370.

(24) Su, X.; Cremer, P. S.; Shen, Y. R.; Somorjai, G. A. High-Pressure CO Oxidation on Pt(111) Monitored with Infrared−Visible Sum Frequency Generation (SFG). *J. Am. Chem. Soc.* **1997**, *119*, 3994−4000.

(25) Klünker, C.; Balden, M.; Lehwald, S.; Daum, W. CO Stretching Vibrations on Pt(111) and Pt(110) Studied by Sumfrequency Generation. *Surf. Sci.* **1996**, *360*, 104−111.

(26) Hayden, B.; Bradshaw, A. The Adsorption of CO on Pt (111) Studied by Infrared-Reflection-Adsorption Spectroscopy. *J. Electron Spectrosc. Relat. Phenom.* **1983**, *30*, 51.

(27) Hayden, B. E.; Kretzschmar, K.; Bradshaw, A. M.; Greenler, R. G. An Infrared Study of the Adsorption of CO on a Stepped Platinum Surface. *Surf. Sci.* **1985**, *149*, 394−406.

(28) McCrea, K.; Parker, J. S.; Chen, P.; Somorjai, G. Surface Structure Sensitivity of High-Pressure CO Dissociation on Pt(5 5 7), Pt(1 0 0) and Pt(1 1 1) Using Sum Frequency Generation Surface Vibrational Spectroscopy. *Surf. Sci.* **2001**, *494*, 238−250.

(29) Schweizer, E.; Persson, B. N. J.; Tüshaus, M.; Hoge, D.; Bradshaw, A. M. The Potential Energy Surface, Vibrational Phase Relaxation and the Order-Disorder Transition in the Adsorption System Pt{111}-CO. *Surf. Sci.* **1989**, *213*, 49−89.

(30) Crossley, A.; King, D. A. Adsorbate Island Dimensions and Interaction Energies from Vibrational Spectra: Co on Pt {001} and Pt {111}. *Surf. Sci.* **1980**, *95*, 131−155.

(31) Busson, B.; Tadjeddine, A. Non-Uniqueness of Parameters Extracted from Resonant Second-Order Nonlinear Optical Spectroscopies. *J. Phys. Chem. C* **2009**, *113*, 21895−21902.

(32) Morkel, M.; Rupprechter, G.; Freund, H.-J. Finite Size Effects on Supported Pd Nanoparticles: Interaction of Hydrogen with CO and C2H4. *Surf. Sci.* **2005**, *588*, L209−L219.

(33) Morkel, M.; Unterhalt, H.; Klüner, T.; Rupprechter, G.; Freund, H.-J. Interpreting Intensities in Vibrational Sum Frequency Generation (SFG) Spectroscopy: CO Adsorption on Pd Surfaces. *Surf. Sci.* **2005**, *586*, 146−156.

(34) Singh, N. B.; Sarkar, U. Structure, Vibrational, and Optical Properties of Platinum Cluster: A Density Functional Theory Approach. *J. Mol. Model.* **2014**, *20*, 2537.

(35) Backus, E. H. G. Real-Time Observation of Molecular Motion on a Surface. *Science* **2005**, *310*, 1790−1793.

(36) Corva, M.; Feng, Z.; Dri, C.; Salvador, F.; Bertoch, P.; Comelli, G.; Vesselli, E. Carbon Dioxide Reduction on Ir(111): Stable Hydrocarbon Surface Species at near-Ambient Pressure. *Phys. Chem. Chem. Phys.* **2016**, *18*, 6763−6772.

(37) Grånäs, E.; Andersen, M.; Arman, M. A.; Gerber, T.; Hammer, B.; Schnadt, J.; Andersen, J. N.; Michely, T.; Knudsen, J. CO Intercalation of Graphene on Ir(111) in the Millibar Regime. *J. Phys. Chem. C* **2013**, *117*, 16438−16447.

(38) Grånäs, E.; Knudsen, J.; Schröder, U. a.; Gerber, T.; Busse, C.; Arman, M. a.; Schulte, K.; Andersen, J. N.; Michely, T. Oxygen Intercalation under Graphene on Ir(111): Energetics, Kinetics, and the Role of Graphene Edges. *ACS Nano* **2012**, *6*, 9951−9963.

(39) Andersen, M.; Hornekær, L.; Hammer, B. Understanding Intercalation Structures Formed under Graphene on Ir(111). *Phys. Rev. B: Condens. Matter Mater. Phys.* **2014**, *90*, 155428.

(40) Cavallin, A.; Pozzo, M.; Africh, C.; Baraldi, A.; Vesselli, E.; Dri, C.; Comelli, G.; Larciprete, R.; Lacovig, P.; Lizzit, S. Local Electronic Structure and Density of Edge and Facet Atoms at Rh Nanoclusters Self-Assembled on a Graphene Template. *ACS Nano* **2012**, *6*, 3034.

(41) Roiaz, M.; Monachino, E.; Dri, C.; Greiner, M.; Knop-Gericke, A.; Schlögl, R.; Comelli, G.; Vesselli, E. Reverse Water−Gas Shift or Sabatier Methanation on Ni(110)? Stable Surface Species at Near-Ambient Pressure. *J. Am. Chem. Soc.* **2016**, *138*, 4146−4154.

(42) Lambert, A. G.; Davies, P. B.; Neivandt, D. J. Implementing the Theory of Sum Frequency Generation Vibrational Spectroscopy: A Tutorial Review. *Appl. Spectrosc. Rev.* **2005**, *40*, 103−145.

(43) Tian, C. S.; Shen, Y. R. Recent Progress on Sum-Frequency Spectroscopy. *Surf. Sci. Rep.* **2014**, *69*, 105−131.

(44) Vidal, F.; Tadjeddine, A. Sum-Frequency Generation Spectroscopy of Interfaces. *Rep. Prog. Phys.* **2005**, *68*, 1095−1127.

(45) Bonn, M.; Hess, C.; Roeterdink, W. G.; Ueba, H.; Wolf, M. Dephasing of Vibrationally Excited Molecules at Surfaces: CO/Ru(001). *Chem. Phys. Lett.* **2004**, *388*, 269−273.

(46) Huang, J.; Shen, Y. Theory of Doubly Resonant Infrared-Visible Sum-Frequency and Difference-Frequency Generation from Adsorbed Molecules. *Phys. Rev. A: At., Mol., Opt. Phys.* **1994**, *49*, 3973−3981.

(47) Velarde, L.; Wang, H.-F. Unified Treatment and Measurement of the Spectral Resolution and Temporal Effects in Frequency-Resolved Sum-Frequency Generation Vibrational Spectroscopy (SFG-VS). *Phys. Chem. Chem. Phys.* **2013**, *15*, 19970−19984.

(48) Mifflin, A. L.; Velarde, L.; Ho, J.; Psciuk, B. T.; Negre, C. F. a.; Ebben, C. J.; Upshur, M. A.; Lu, Z.; Strick, B. L.; Thomson, R. J.; et al. Accurate Line Shapes from Sub-Cm $^{-1}$ Resolution Sum Frequency Generation Vibrational Spectroscopy of α-Pinene at Room Temperature. *J. Phys. Chem. A* **2015**, *119*, 1292−1302.

(49) Doniach, S.; Sunjic, M. Many-Electron Singularity in X-Ray Photoemission and X-Ray Line Spectra from Metals. *J. Phys. C: Solid State Phys.* **1970**, *3*, 285−291.

(50) Hattab, H.; N'Diaye, a. T.; Wall, D.; Jnawali, G.; Coraux, J.; Busse, C.; van Gastel, R.; Poelsema, B.; Michely, T.; Meyer zu Heringdorf, F.-J.; et al. Growth Temperature Dependent Graphene Alignment on Ir(111). *Appl. Phys. Lett.* **2011**, *98*, 141903.

(51) N'Diaye, A. T.; Bleikamp, S.; Feibelman, P. J.; Michely, T. Two-Dimensional Ir Cluster Lattice on a Graphene Moiré on Ir(111). *Phys. Rev. Lett.* **2006**, *97*, 215501.

(52) Giannozzi, P.; Baroni, S.; Bonini, N.; Calandra, M.; Car, R.; Cavazzoni, C.; Ceresoli, D.; Chiarotti, G. L.; Cococcioni, M.; Dabo, I.;

et al. QUANTUM ESPRESSO: A Modular and Open-Source Software Project for Quantum Simulations of Materials. *J. Phys.: Condens. Matter* **2009**, *21*, 395502.

(53) Perdew, J. P.; Burke, K.; Ernzerhof, M. Generalized Gradient Approximation Made Simple. *Phys. Rev. Lett.* **1996**, *77*, 3865−3868.

(54) Grimme, S. Semiempirical GGA-Type Density Functional Constructed with a Long-Range Dispersion Correction. *J. Comput. Chem.* **2006**, *27*, 1787−1799.

(55) Andersen, J.; Hennig, D.; Lundgren, E.; Methfessel, M.; Nyholm, R.; Scheffler, M. Surface Core-Level Shifts of Some 4d-Metal Single-Crystal Surfaces: Experiments and *Ab Initio* Calculations. *Phys. Rev. B: Condens. Matter Mater. Phys.* **1994**, *50*, 17525−17533.

(56) N'Diaye, A. T.; Coraux, J.; Plasa, T. N.; Busse, C.; Michely, T. Structure of Epitaxial Graphene on Ir(111). *New J. Phys.* **2008**, *10*, 043033.

(57) Monkhorst, H. J.; Pack, J. D. Special Points for Brillouin-Zone Integrations. *Phys. Rev. B* **1976**, *13*, 5188−5192.

(58) Tersoff, J.; Hamann, D. R. Theory of the Scanning Tunneling Microscope. *Phys. Rev. B: Condens. Matter Mater. Phys.* **1985**, *31*, 805−813.

(59) Corva, M.; Vesselli, E. Room Temperature Carbonylation of Iron−Phthalocyanines Adsorbed on a Single Crystal Metal Surface: An *in Situ* SFG Investigation at Near-Ambient Pressure. *J. Phys. Chem. C* **2016**, *120*, 22298−22303.

Experimental and Theoretical Investigation of the Restructuring Process Induced by CO at Near Ambient Pressure: Pt Nanoclusters on Graphene/Ir(111)

Nicola Podda,[†] Manuel Corva,[†,‡] Fatema Mohamed,[†,§] Zhijing Feng,[†,‡] Carlo Dri,[†,‡] Filip Dvorák,[#] Vladimir Matolin,[#] Giovanni Comelli,[†,‡] Maria Peressi,[†,‡] and Erik Vesselli[†,‡,*]

[†]Physics Department, University of Trieste, via A. Valerio 2, 34127 Trieste, Italy

[‡]Istituto Officina dei Materiali CNR-IOM, S.S. 14 km 163.5, Area Science Park, 34149 Basovizza (Trieste), Italy

[§]International Centre for Theoretical Physics ICTP, Strada Costiera 11, 34151 Trieste, Italy

[#]Charles University in Prague, Faculty of Mathematics and Physics, V Holešovickách 2, 180 00 Praha 8, Czech Republica

Supporting Information
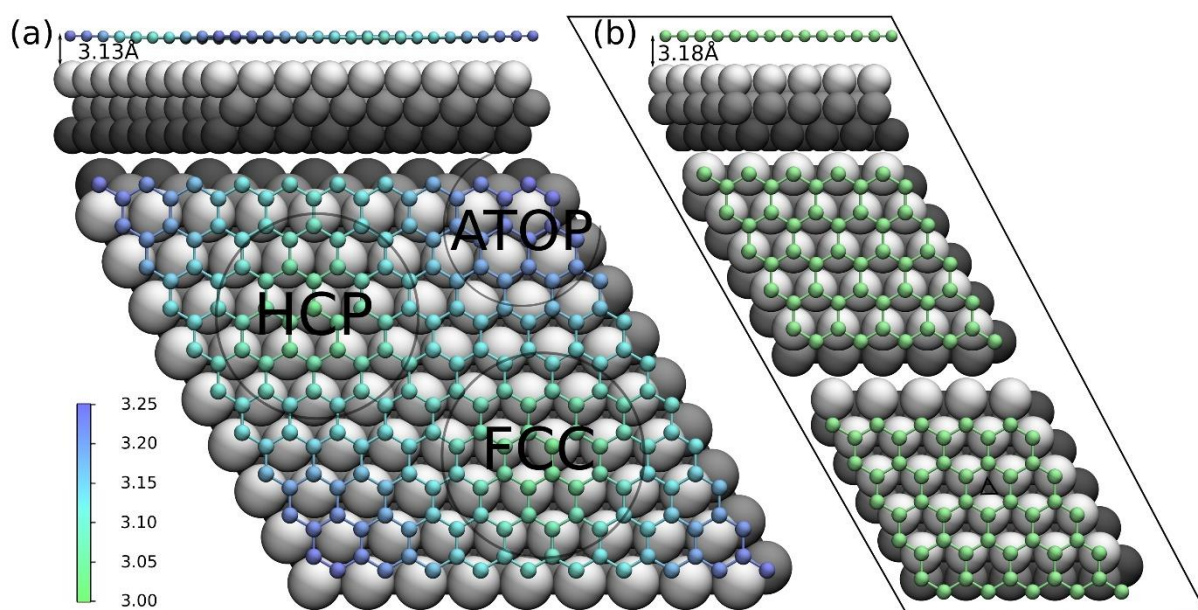
Figure S1. (a) Optimized structure for the full model of the graphene Moiré on Ir(111) described by a GR(10 × 10)/Ir(9 × 9) supercell and (b) the reduced models for the HCP and FCC regions, described by two different GR(5 × 5)/Ir(5 × 5) supercells. The color scale of the C atoms in (a) maps the distance with respect to the Ir-substrate: the average graphene distance from the Ir substrate is 3.13 Å in the full model and 3.18 Å (constant value) in the reduced models.
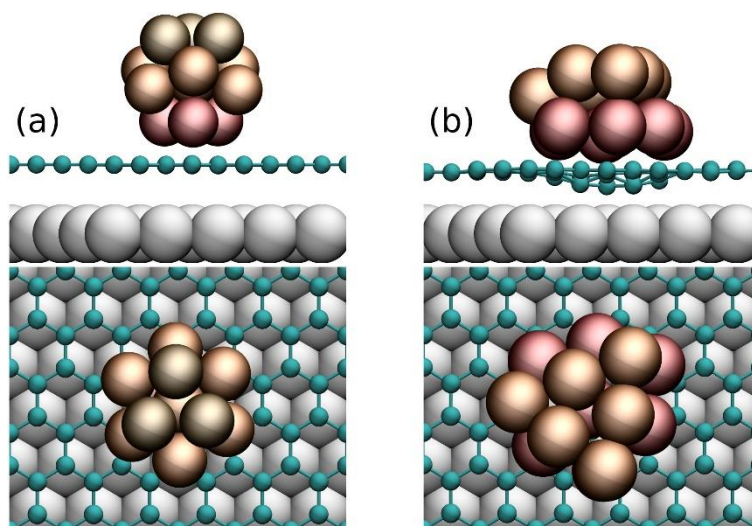
Figure S2. Initial configuration (a) of a spherical Pt_{13} nanocluster on GR/Ir(111) and its optimized structure after relaxation (b), suggesting the trend of nanoclusters with few Pt atoms to wet the GR layer. See caption of Figure S1 for the color scale.
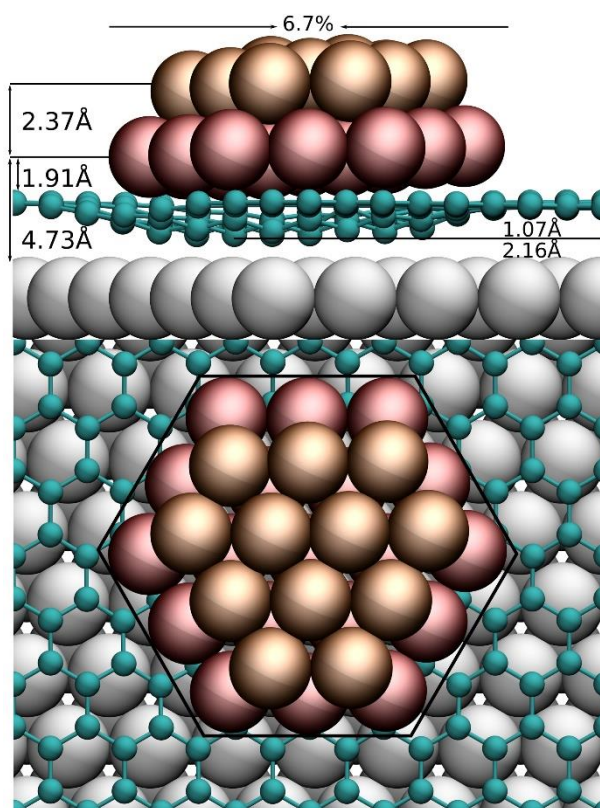
Figure S3. Fully optimized structure of the 31 atoms Pt cluster on the HCP region of the Moiré. The 19 Pt atoms in the 1st layer (red) host the 12 atoms in the 2nd layer (orange).
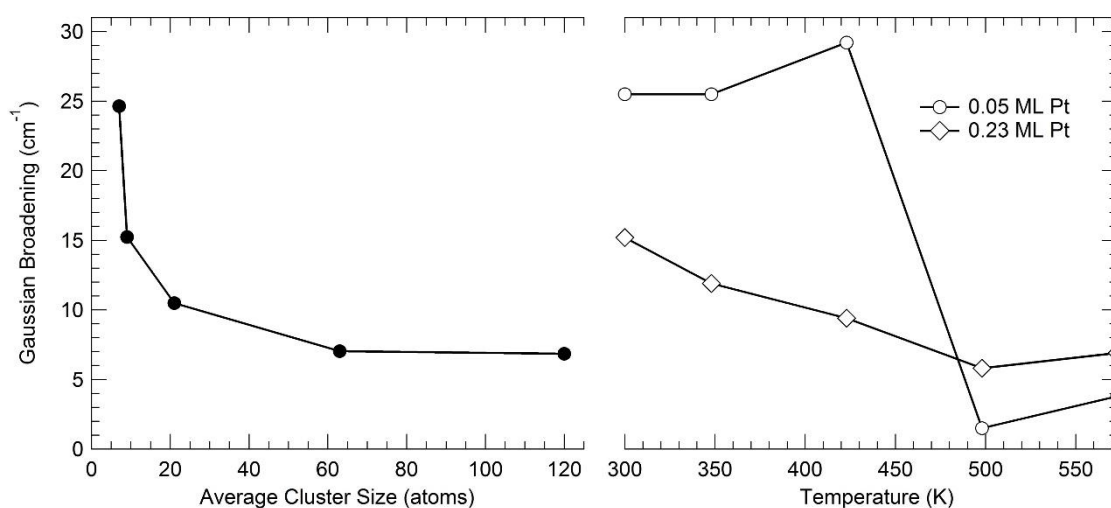
Figure S4. Gaussian broadening of the IR-vis SFG resonances, obtained from the fitting procedure, as a function of the Pt clusters size at room temperature (left), and as a function of the temperature (right).
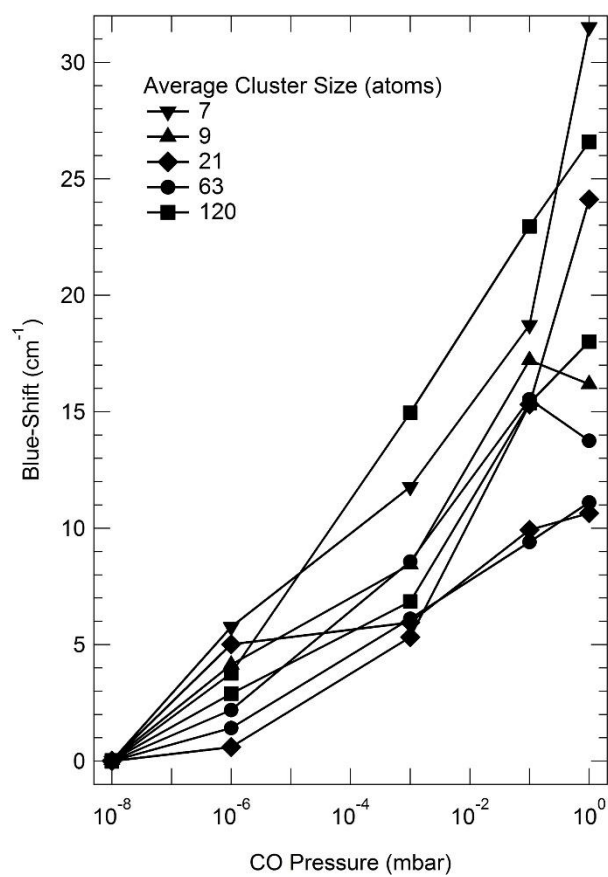
Figure S5. Blue-shift of the IR-vis SFG resonances as a function of the CO pressure for different clusters sizes.
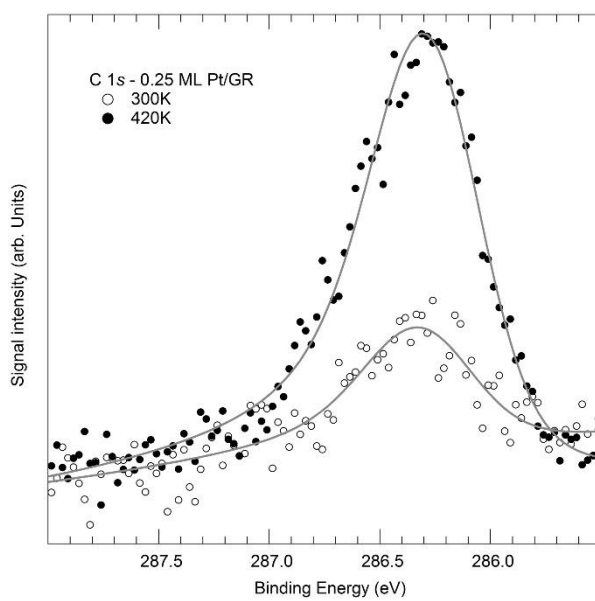
Figure S6. C 1*s* core level spectra in the CO region at 0.1 mbar CO for the 0.25 ML Pt/GR system.
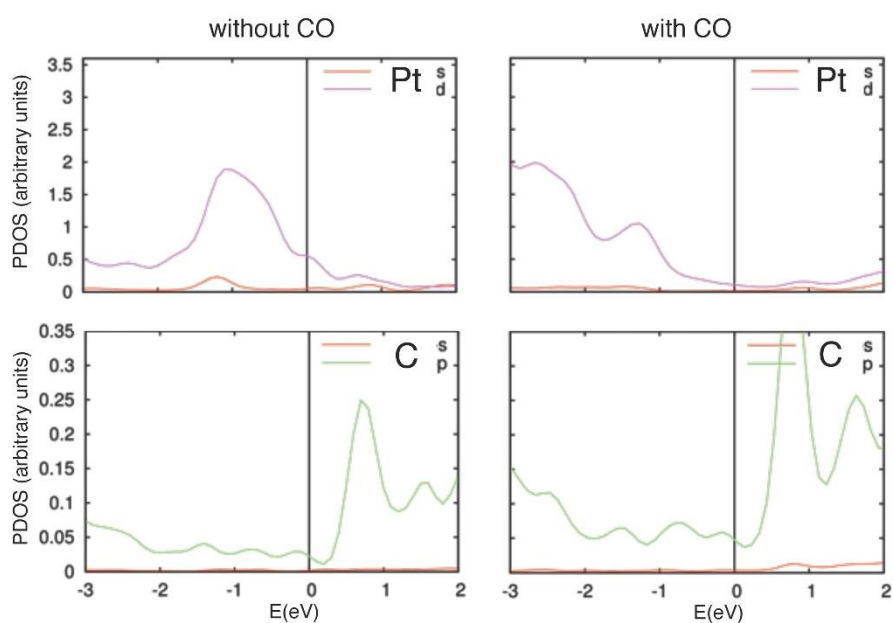
Figure S7. Projected Density Of States (PDOS) for selected atoms of the Pt_{19} nanocluster with (right) and without (left) adsorbed CO molecules. Upper panels: Pt atom at the center of the nanocluster, which upon CO adsorption is pulled up and detached from graphene. Lower panels: C atom of graphene beneath that specific Pt atom.

Parameter	CO Pressure (mbar)				
	10^{-8}	10^{-6}	10^{-3}	10^{-1}	10^{0}
$A^{(NR)}$ (arb. units)	0.98	0.97	0.96	0.96	0.99
Gauss σ (cm^{-1})	24	24	27	24	24
$A_1^{(RES)}$ (arb. units)	-	-	-	0.93	0.93
$\Delta\varphi_1$ (°)	-	-	-	312	312
ω_1 (cm^{-1})	-	-	-	1845	1845
Γ_1 (cm^{-1})	-	-	-	7.2	7.2
$A_2^{(RES)}$ (arb. units)	6.5	4.7	2.5	6.2	3.4
$\Delta\varphi_2$ (°)	253	253	253	253	253
ω_2 (cm^{-1})	1975	1965	2002	2000	1952
Γ_2 (cm^{-1})	23	23	23	23	23
$A_3^{(RES)}$ (arb. units)	19	18	19	19	17
$\Delta\varphi_3$ (°)	73	73	73	73	73
ω_3 (cm^{-1})	2039	2045	2051	2058	2071
Γ_3 (cm^{-1})	24	24	24	24	24

Table S1. 0.05 ML Pt as a function of the CO pressure at room temperature: best fitting parameters of the spectra shown in Figure 5.

Parameter	CO Pressure (mbar)				
	10^{-8}	10^{-6}	10^{-3}	10^{-1}	10^{0}
$A^{(NR)}$ (arb. units)	0.99	0.99	1.0	1.0	0.99
Gauss σ (cm^{-1})	15	15	15	15	15
$A_1^{(RES)}$ (arb. units)	2.1	0.67	1.3	2.2	1.5
$\Delta\varphi_1$ (°)	143	143	143	143	143
ω_1 (cm^{-1})	1871	1871	1871	1865	1877
Γ_1 (cm^{-1})	7.2	7.2	7.2	7.2	7.2
$A_2^{(RES)}$ (arb. units)	3.4	1.6	2.7	2.3	4.0
$\Delta\varphi_2$ (°)	272	272	272	272	272
ω_2 (cm^{-1})	1969	1950	1980	1990	1993
Γ_2 (cm^{-1})	23	23	23	23	23
$A_3^{(RES)}$ (arb. units)	15	17	15	15	14
$\Delta\varphi_3$ (°)	67.8	67.8	67.8	67.8	67.8
ω_3 (cm^{-1})	2041	2046	2049	2058	2057
Γ_3 (cm^{-1})	22	22	22	22	22

Table S2. 0.09 ML Pt as a function of the CO pressure at room temperature: best fitting parameters of the spectra shown in Figure 5.

Parameter	CO Pressure (mbar)				
	10^{-8}	10^{-6}	10^{-3}	10^{-1}	10^{0}
$A^{(NR)}$ (arb. units)	0.99	1.0	0.99	0.97	0.97
Gauss σ (cm^{-1})	11	9.7	10	11	11
$A_1^{(RES)}$ (arb. units)	-	0.22	-	1.2	1.6
$\Delta\varphi_1$ (°)	-	9	-	9	9
ω_1 (cm^{-1})	-	1856	-	1837	1833
Γ_1 (cm^{-1})	-	7.2	-	7.2	7.2
$A_2^{(RES)}$ (arb. units)	9.1	9.4	8.6	8.6	7.4
$\Delta\varphi_2$ (°)	296	295	260	260	273
ω_2 (cm^{-1})	1982	1989	1982	1982	1992
Γ_2 (cm^{-1})	23	24	21	21	21
$A_3^{(RES)}$ (arb. units)	10	8.2	8.1	6.7	5.9
$\Delta\varphi_3$ (°)	63	68	68	68	87
ω_3 (cm^{-1})	2014	2015	2019	2030	2039
Γ_3 (cm^{-1})	19	18	13	13	14
$A_4^{(RES)}$ (arb. units)	13	16	16	12	12
$\Delta\varphi_4$ (°)	53	51	38	28	27
ω_4 (cm^{-1})	2076	2081	2082	2086	2086
Γ_4 (cm^{-1})	18	18	16	12	12

Table S3. 0.25 ML Pt as a function of the CO pressure at room temperature: best fitting parameters of the spectra shown in Figure 5.

Parameter	CO Pressure (mbar)				
	10^{-8}	10^{-6}	10^{-3}	10^{-1}	10^{0}
$A^{(NR)}$ (arb. units)	1.03	1.03	0.97	0.90	0.93
Gauss σ (cm^{-1})	7.2	7.5	7.7	7.2	5.6
$A_1^{(RES)}$ (arb. units)	-	0.40	0.73	2.8	2.7
$\Delta\varphi_1$ (°)	-	352	352	352	352
ω_1 (cm^{-1})	-	1840	1840	1840	1841
Γ_1 (cm^{-1})	-	7.2	7.2	7.2	7.2
$A_2^{(RES)}$ (arb. units)	16	18	19	19	15
$\Delta\varphi_2$ (°)	279	279	279	279	279
ω_2 (cm^{-1})	1989	1994	1996	2002	2007
Γ_2 (cm^{-1})	23	23	23	23	23
$A_3^{(RES)}$ (arb. units)	24	27	27	30	22
$\Delta\varphi_3$ (°)	229	229	229	229	229
ω_3 (cm^{-1})	2033	2035	2041	2048	2046
Γ_3 (cm^{-1})	14	14	14	14	14
$A_4^{(RES)}$ (arb. units)	52	46	47	51	59
$\Delta\varphi_4$ (°)	8	357	353	343	343
ω_4 (cm^{-1})	2068	2069	2074	2077	2079
Γ_4 (cm^{-1})	17	14	13	13	16

Table S4. 0.75 ML Pt as a function of the CO pressure at room temperature: best fitting parameters of the spectra shown in Figure 5.

Parameter	CO Pressure (mbar)				
	10^{-8}	10^{-6}	10^{-3}	10^{-1}	10^{0}
$A^{(NR)}$ (arb. units)	0.92	0.95	0.91	1.00	0.94
Gauss σ (cm^{-1})	6.7	6.5	7.1	7.0	7.0
$A_1^{(RES)}$ (arb. units)	-	-	-	13	13
$\Delta\varphi_1$ (°)	-	-	-	65	65
ω_1 (cm^{-1})	-	-	-	1850	1856
Γ_1 (cm^{-1})	-	-	-	22	22
$A_2^{(RES)}$ (arb. units)	6.4	6.4	7.6	20	15
$\Delta\varphi_2$ (°)	351	351	351	351	351
ω_2 (cm^{-1})	2011	2011	2038	2035	2035
Γ_2 (cm^{-1})	15	15	15	15	15
$A_3^{(RES)}$ (arb. units)	21	18	26	63	23
$\Delta\varphi_3$ (°)	221	229	229	223	223
ω_3 (cm^{-1})	2030	2034	2045	2053	2057
Γ_3 (cm^{-1})	7.6	8.5	8.5	15	15
$A_4^{(RES)}$ (arb. units)	106	102	104	93	73
$\Delta\varphi_4$ (°)	348	344	344	343	343
ω_4 (cm^{-1})	2066	2069	2073	2081	2084
Γ_4 (cm^{-1})	12	11	11	11	11

Table S5. 1.5 ML Pt as a function of the CO pressure at room temperature: best fitting parameters of the spectra shown in Figure 5.

Parameter	Temperature (K)				
	300	350	425	500	575
$A^{(NR)}$ (arb. units)	1.00	0.98	1.00	1.00	1.00
Gauss σ (cm^{-1})	26	29	29	1.5	3.8
$A_1^{(RES)}$ (arb. units)	0.93	0.93	5.0	16	-
$\Delta\varphi_1$ (°)	312	312	312	210	-
ω_1 (cm^{-1})	1850	1883	1889	1834	-
Γ_1 (cm^{-1})	7.2	7.2	7.2	5.2	-
$A_2^{(RES)}$ (arb. units)	5.5	4.7	12	2.0	0.61
$\Delta\varphi_2$ (°)	229	229	229	279	189
ω_2 (cm^{-1})	1984	1981	1956	1970	1946
Γ_2 (cm^{-1})	23	23	23	24	24
$A_3^{(RES)}$ (arb. units)	15	13	17	-	-
$\Delta\varphi_3$ (°)	67.8	67.8	67.8	-	-
ω_3 (cm^{-1})	2041	2046	2049	-	-
Γ_3 (cm^{-1})	22	22	22	-	-
$A_5^{(RES)}$ (arb. units)	-	-	-	37	37
$\Delta\varphi_5$ (°)	-	-	-	331	328
ω_5 (cm^{-1})	-	-	-	2051	2043
Γ_5 (cm^{-1})	-	-	-	10	10

Table S6. 0.05 ML Pt in 0.1 mbar CO as a function of temperature: best fitting parameters of the spectra shown in Figure 7.

Parameter	Temperature (K)				
	300	350	425	500	575
$A^{(NR)}$ (arb. units)	1.00	1.00	1.05	1.04	1.04
Gauss σ (cm^{-1})	15	12	9.4	5.8	6.9
$A_1^{(RES)}$ (arb. units)	2.0	-	-	-	-
$\Delta\varphi_1$ (°)	9	-	-	-	-
ω_1 (cm^{-1})	1838	-	-	-	-
Γ_1 (cm^{-1})	7	-	-	-	-
$A_2^{(RES)}$ (arb. units)	7.3	4.5	8.4	5.6	2.9
$\Delta\varphi_2$ (°)	280	280	283	291	261
ω_2 (cm^{-1})	1983	1975	1984	1983	1955
Γ_2 (cm^{-1})	23	23	23	23	23
$A_3^{(RES)}$ (arb. units)	10	10	7.0	-	-
$\Delta\varphi_3$ (°)	61	61	61	-	-
ω_3 (cm^{-1})	2036	2031	2024	-	-
Γ_3 (cm^{-1})	14	14	14	-	-
$A_4^{(RES)}$ (arb. units)	15	15	-	-	-
$\Delta\varphi_4$ (°)	70	35	-	-	-
ω_4 (cm^{-1})	2093	2076	-	-	-
Γ_4 (cm^{-1})	15	11	-	-	-
$A_5^{(RES)}$ (arb. units)	-	-	22	32	31
$\Delta\varphi_5$ (°)	-	-	347	340	334
ω_5 (cm^{-1})	-	-	2057	2050	2040
Γ_5 (cm^{-1})	-	-	8.6	11	10
$A_6^{(RES)}$ (arb. units)	-	-	6.8	6.6	7.4
$\Delta\varphi_6$ (°)	-	-	173	167	168
ω_6 (cm^{-1})	-	-	1870	1881	1879
Γ_6 (cm^{-1})	-	-	22	22	25

Table S7. 0.25 ML Pt in 0.1 mbar CO as a function of temperature: best fitting parameters of the spectra shown in Figure 7.

Parameter	System			
	GR @ RT	GR @ 420 K	0.25 ML Pt/GR @ RT	0.25 ML Pt/GR @ 420 K
Lor width (eV)	0.11	0.11	0.11 (0.23)	0.11
Gauss width (eV)	0.40	0.47	0.40 (0.80)	0.41
Asymm.	0.1	0.1	0.1 (0.0)	0.1
Intensity (arb. units)	3.4	3.3	2.0 (0.8)	3.3
BE (eV)	284.1	284.1	284.0 (284.2)	283.8

Table S8. Fitting parameters of the C 1*s* core level spectra of graphene shown in Figure 9 (values in parenthesis are related to the broad shoulder that develops at room temperature).

Parameter	System	
	0.25 ML Pt/GR @ RT	0.25 ML Pt/GR @ 420 K
Lor width (eV)	0.19	0.19
Gauss width (eV)	0.58	0.58
Asymm.	0.1	0.1
Intensity (arb. units)	0.8	0.9
BE (eV)	71.10	71.10
Intensity (arb. units)	0.7	0.4
BE (eV)	71.70	71.70
Intensity (arb. units)	0.3	0.1
BE (eV)	72.15	72.15

Table S9. Fitting parameters of the Pt 4$f_{7/2}$ core level spectra shown in Figure 9.